Multiphase Computational Fluid Dynamics Modelling of Gas Liquid Separation in an Ebullated Bed Hydroprocessor

Katelyn Evans

Thesis submitted to the University of Ottawa
in partial Fulfillment of the requirements for the
Master of Applied Science in Chemical Engineering

Department of Chemical and Biological Engineering
Faculty of Engineering
University of Ottawa

© Katelyn Evans, Ottawa, Canada, 2024

Abstract

This research built a multiphase computational fluid dynamics model for the gas-liquid separator in an ebullated bed hydroprocessor. The k-ω Shear Stress Transport turbulence model in conjunction with the Tomiyama slightly contaminated drag model were used to investigate gas-liquid separation efficiency. Strategic model selection ensures stable and accurate results, laying groundwork for future model comparisons incorporating inhomogeneous multiple size group population balance models. Case studies explore impacts of independent variables on separation efficiency, revealing that larger bubble size enhances separation by facilitating disengagement from liquid streamlines. Augmenting inlet gas phase fraction increases overall gas holdup, reduces mean liquid residence time and separation efficiency. A greater liquid momentum's effect on residence time is less pronounced but decreases separation efficiency. Viscosity inversely affects separation efficiency due to decreased relative velocities. Increasing liquid recycle ratio decreases separation efficiency by reducing mean liquid residence time. Mean liquid residence time emerges as a reliable predictor of separation efficiency, underscoring its significance in process optimization. Future inclusion of population balance models could provide insights into the impact of different bubble sizes and breakup/coalescence modeling, with validation challenges anticipated. Additionally, incorporating turbulence models accommodating phase inversion phenomena shows promise in improving simulation robustness, especially in complex scenarios like population balance models, warranting further investigation for accurate phase inversion dynamics capture.

Statement of Contributions

I, Katelyn Evans, affirm that this thesis titled “Multiphase Computational Fluid Dynamics Modelling of Gas Liquid Separation in an Ebullated Bed Hydroprocessor” is entirely my own work, encompassing conception, design, execution, and interpretation of research findings. While I declare sole authorship, I acknowledge the invaluable guidance of my co-supervisors Dr. Jan Haelssig and Dr. Arturo Macchi, who provided editorial comments and corrections.

Acknowledgements

I would like to express my deepest gratitude to Dr. Jan Haelssig for his invaluable guidance, unwavering support, and expert mentorship throughout the course of this research. His profound insights into CFD modeling and computational techniques have been instrumental in shaping the trajectory of this work. I am profoundly grateful for his dedication, patience, and encouragement, which have been indispensable in navigating the complexities of the study.

I am also indebted to Dr. Arturo Macchi for his expertise, and invaluable contributions to this endeavor. Dr. Macchi's profound understanding of fluid dynamics has enriched our discussions and provided invaluable perspectives. I extend my heartfelt appreciation to him for offering me this opportunity, for his continual guidance, and for his unwavering belief in this project.

I would like to extend my sincere gratitude to Syncrude for their generous funding, which made this research possible. Their support has been instrumental in advancing our understanding in this field and driving innovation forward.

I am deeply thankful to Dr. Jason Wiens and Dr. John Adjaye from Syncrude for their instrumental role in facilitating this collaboration and for their invaluable insights throughout the project. Their expertise and guidance have been invaluable assets, shaping the direction of this research and enriching its outcomes.

Table of Contents

List of Figures

List of Tables

List of Abbreviations

Variable		
C_d	Drag Coefficient	-
C_I	Modulation Parameter	-
C_L	BIT Model Coefficient	-
C_L	Lift Coefficient	-
C_{VM}	Virtual Mass Coefficient	-
C_ε	Dissipation Coefficient	-
$C_{\omega D}$	BIT Model Coefficient	-
C_μ	BIT Model Coefficient	-
C_ω^{RANS}	BIT Model Coefficient	-
d_b	Bubble Diameter	m
D_k^{RANS}	Turbulent Dissipation Term	kg m^{-1} s^{-4}
Eo	Eötvös Number	-
F_B	Buoyant Force	N
F_D	Drag Force	N
F_L	Lift Force	N
F_{TD}	Turbulent Dispersion Force	N
F_{VM}	Virtual Mass Force	N
F_{WL}	Wall Lubrication Force	N
g	Acceleration due to gravity	m s^{-2}
I	Identity Matrix	-
k	Turbulent Kinetic Energy	m^2 s^{-2}
l	Turbulent Length	m
$\dot{m}$	Mass Flow Rate	kg m^{-3}
$\vec{M}$	Volumetric Interfacial Forces Vector	N m^{-3}
n	direction normal to the boundary	-
P	Pressure	Pa
Q	Volumetric Flow Rate	m^3 s
R	Radius	m
$\mathcal{R}$	Recycle Ratio	-
$\mathbf{R}$	Reynolds Stress	Pa
Re	Reynolds Number	-
S	Momentum source vector	-
S_ε^{RANS}	BIT Interfacial Energy Dissipation	kg m^2 s^{-3}
S_k^{RANS}	BIT Interfacial Energy Transfer	kg m^2 s^{-2}
t	Time	s
U_{rel}	Relative Velocity	m s^{-1}
$\vec{U}$	Velocity vector	m s^{-1}
V	Volume	m^3
y	Distance from wall	-
Π_k^{RANS}	Turbulent Production Term	kg m^{-1} s^{-3}

Greek Letter		
α	Volume fraction	-
ρ	Density	kg m^{-3}
τ	Shear Tensor	Pa
μ	Dynamic Viscosity	N s^{1} m^{-2}
σ_{TD}	Turbulent Schmidt Number	-
ω	Rate of Dissipation of Turbulent Kinetic Energy	s^{-1}
ν	Kinematic Viscosity	m^2 s
ε	Turbulent Dissipation Rate	m^2 s^{-3}
η	Separation Efficiency	-
ϕ	Generic Flow Variable of Interest	-
Subscript		
l	Liquid	-
b	Bubble	-
c	Continuous	-
d	Dispersed phase	-
g	Gas	-
j	General phase	-
$turb$	Turbulent	-
Superscript		
-	Time Averaged Quantity	-
‘	Turbulent Fluctuation	-
Abbreviations		
EBHR	Ebullated Bed Hydroprocessor	-
CFD	Computational Fluid Dynamics	-
DNS	Direct Numerical Simulation	-
LES	Large Eddy Simulation	-
RANS	Reynolds Averaged Navier Stokes	-
BIT	Bubble Induced Turbulence	-
FVM	Finite Volume Method	-
PISO	Pressure-Implicit Split-Operator	-
SIMPLE	Semi-Implicit Method for Pressure-Linked	-

Chapter 1

Introduction

1.1 Oil and Gas Upgrading in the Alberta Oil Sands

Canada is home to many natural resources among them the third largest globally proven oil reserve, principally located in the Western provinces of Alberta and Saskatchewan (the oil sands account for 91% of Canada's oil reserve) (Government of Canada, 2019). Canada's oil production is expected to experience economic growth over the next 25 years. However, innovation is critical and ongoing to reduce the carbon footprint of the extraction, upgrading and refining processes (Government of Canada, 2020).

One company committed to research and development in the Canadian oil sands is Syncrude; a joint venture project operated by Suncor. Syncrude operates 2 mines: Mildred Lake and Aurora both located in Fort McMurray, Alberta (Syncrude, 2020). Once the oil sands are mined a water frothing technique is used to extract the bitumen. Recovered bitumen is sent to the upgraders, primarily distillation towers operated under atmospheric and vacuum conditions (Mach et al., 2020a). Wherein hydrocarbons with a lower boiling point are recovered as products in the gaseous state and the heavy gas oils exit as a liquid, which are further processed in the upgrading units. The upgrading process is done either through a carbon rejection process in the Fluid Cokers or a hydrogen addition process in the LC-Fining^{TM} unit, which will be focus of this report. Products from the LC-Fining^{TM} unit, Cokers and Distillation towers are sent to the hydrotreaters which remove any remaining impurities including sulfur and then converted into Syncrude Sweet Blend, a synthetic crude oil (Lane et al., 2019a).

Commercially operated ebullated-bed reactors, such as Syncrude's LC-Fining^{TM} units, are commonly used to convert petroleum distillation residues into high-quality products (Eccles, 1993). LC-Fining^{TM} unit take heavy gas oil products bitumen residue from distillation towers mixed with hydrogen rich treat gas and a liquid recycle stream. The gas-liquid mixture is uniformly distributed into the catalyst bed through a bubble capped grid plate (Lane et al., 2019b). Above the

grid plate is the catalyst bed, as the catalyst ages it can be replaced during the run as the reactor is specifically designed for catalyst addition and withdraw (Eccles, 1993). The LC-Fining^{TM} unit is an integral part of the Syncrude upgrading processes, additional knowledge regarding the gas-liquid separation and bubble dynamics throughout the reactor would provide valuable insight on how to optimize the liquid holdup within the bed and therefore increase overall yield.

Gas-liquid systems operating in bubbly flow regime are very common in chemical production, petroleum, and nuclear industries. In the gas-liquid zones of Syncrude's LC-Fining^{TM} units, the reactor operates in multiphase polydisperse mode, where the liquid is the continuous phase and the gas is dispersed. While performing accurate simulation is a complex process it provides insightful information for scale-up and optimization purposes (Buffo et al., 2016). The importance and relevance of computational fluid dynamics (CFD) is only continuing to grow; with increasing computation power simulations can become more accurate on smaller scales (Liao et al., 2015). These advancements have allowed for modelling of bubble size and density distribution, which is a powerful tool to increase the overall yield of Syncrude's LC-Fining^{TM} unit.

1.2 The Physics of LC-Fining

Syncrude's LC-Fining^{TM} units upgrade atmospheric topped bitumen (ATB) and vacuum topped bitumen (VTB) through a hydrogen addition process, via hydrogen rich treat gas (McKnight et al., 2003). The unit consists of 3 main sections: the plenum chamber, the ebullated bed and the freeboard region, see Figure 1.1 (Lane et al., 2016a). The liquid feed and treat gas enter through the distributor ring in the plenum chamber, where they are mixed with the (primarily) liquid recycle. The recycle line is essential to economical operation of the unit, its primary functions are to recycle unconverted liquid (which improves overall yield) and maintain fluidization of the bed (Mach et al., 2020a). Note the primary mechanism for fluidization is via the liquid and not gas in the case of the LC-Fining^{TM} unit. The fluidized bed is operated between 420-450°C within a pressure range of 10-15MPa (Pjontek, 2014). Critical to the optimal operation of the LC-Fining^{TM} unit is the gas-liquid interactions specifically the gas dispersion in the plenum chamber and the gas-liquid separation in the freeboard region, both of which will be discussed in the following sections.

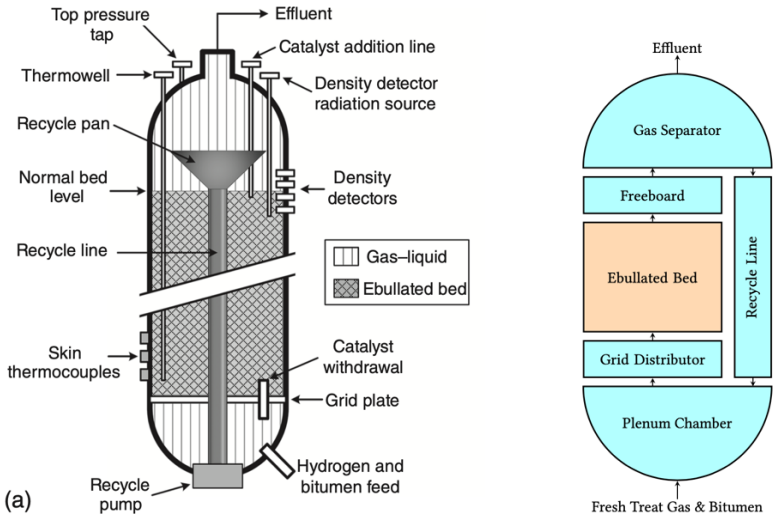

Figure 1.1: LC-Fining^{TM} Unit Schematic. Sourced from (Mach et al., 2020a).

Fresh feed and treat gas enter the LC-Fining^{TM} unit through a distributor ring located in the plenum chamber, where they are mixed with the liquid recycle. The grid-plate, located at the boundary of the plenum and fluidized bed, uses bubble caps to uniformly distribute the gas and liquid into the ebullated bed (Lehnigk et al., 2022). The bubble-cap design dictates the bubble size distribution moreover the size of bubbles sparged into the plenum chamber does not significantly impact the size of bubbles in the ebullated bed (Mach et al., 2020a). Uniform gas-liquid distribution into the catalyst bed region is critical to overall reactor performance and thus is the primary goal of the grid-plate distributor and plenum chamber. However, swirl induced by the liquid recycle causes uneven radial distribution of fluids into the catalyst bed (Mach et al., 2020a) (Song et al., 2014). The periphery risers are flooded with liquid causing the gas pocket to be deeper in the center, see Figure 1.2. Optimizing the operating conditions and design of the plenum chamber, distributor ring and grid-plate, are outside the scope of this work, but studies have been initiated by (Mach et al., 2020a) (Totten, 2019).

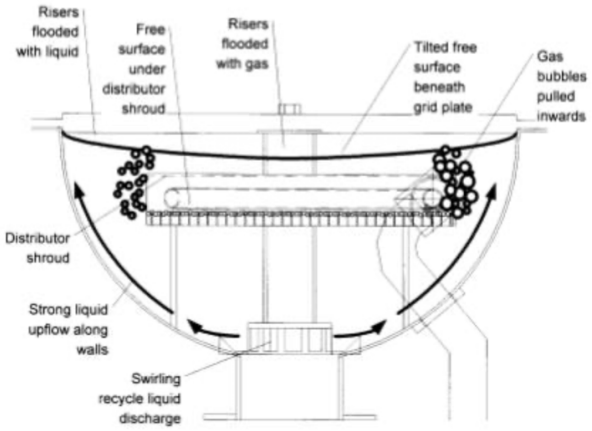

Figure 1.2: Effect of Swirl Induced by Recycle. Sourced from (Pjontek, 2014)

Most of the conversion occurs in the ebullated bed, prior to entering the freeboard region where the separation of liquid and gas is crucial. The catalytic reaction can be described with the following steps (Pjontek et al., 2020).

1. Diffusion from gas to liquid
2. Diffusion from liquid to solid surface
3. Internal diffusion to the catalytic active site
4. Adsorption into the catalytic site
5. Reaction on catalyst
6. Desorption of products
7. Internal diffusion to solid surface
8. Diffusion from solid surface to bulk liquid

Worth noting conversion is expected in the freeboard region due to entrained catalyst and thermal cracking (Eccles, 1993). Additionally, the presence of the catalyst was not found to have significant impact on the overall gas holdup, assuming the slip velocity is near 0, this can be extended to the bubble size distribution (Pjontek, 2014). There are two consequential impacts of this finding, firstly data generated using bubble columns at elevated pressure may be applied to the LC-Fining^{TM} unit and secondly the design of the grid-plate will determine the size of bubbles throughout the entirety of the ebullated bed and freeboard. The operation of the ebullated bed can

be optimized through the liquid hold-up which is enhanced by higher efficiency gas-liquid separation in the freeboard region (Lane et al., 2019b).

The separation of liquid and gas in the freeboard is important not only to improve the single pass conversion, but also to reduce the production of carbonaceous mesophase which causes fouling and non-uniform gas-liquid distribution (Eccles, 1993). The separation of small bubbles (<1mm in diameter) must occur in the freeboard region, if small bubbles enter the recycle it is highly unlikely they will overcome the net downward liquid flow (Lane et al., 2016a). Ideally the recycle line would primarily recycle liquid, which would be used to maintain the fluidized bed and increase overall conversion.

In this study, a multiphase Eulerian Computational Fluid Dynamics (CFD) model is used to investigate the gas-liquid separation efficiency above the recycle pan. The adopted model advances the approach used by Lane et al., 2019a by adding liquid turbulence predictions since it impacts bubble trajectory and residence time by generating secondary flows and vortices, which in turn influence the flow field and the overall gas-liquid separation process. Moreover, an expanded range of operating conditions will be investigated to determine the impact of liquid viscosity and fluids flow rates influence on swirl formation and ultimately separation efficiency (Mowla et al., 2023). Understanding the effects of increased throughput of heavier (e.g., more viscous) bitumen resid fresh feed is of interest to the overall upgrading process to lower environmental impact and increase profitability.

1.3 Multiphase Hydrodynamics Challenges

1.3.1 Turbulence

Single phase fluid flow regime such as laminar or turbulent flow can be classified based off the Reynolds number, Re, a dimensionless parameter. The Reynolds number is defined as follows.

$$\mathrm{Re} = \frac{\rho L U}{\mu} \tag{1.1}$$

$$\mathrm{Re} < 2300 \quad \text{Laminar Regime}$$
$$2300 < \mathrm{Re} < 4000 \quad \text{Transitional Regime}$$
$$\mathrm{Re} > 4000 \quad \text{Turbulent Regime}$$

Where ρ, represents the fluid density, L, the characteristic length, U, the velocity, and μ, the dynamic viscosity. Laminar flow is typically characterized as smooth and ordered flow with a parabolic flow profile. While turbulent flow is characterized as chaotic and disorder flow, with a more blunted flow profile due to enhanced radial mixing. Turbulence develops because of a build-up of momentum with insufficient stabilizing forces, such as frictional forces (Pope, 2020).

When studying separation efficiency, accurately modelling the development of the flow field, is crucial, therefore one of the goals of this work is to improve previous models by incorporating turbulence (Lane et al., 2019b). The type of CFD simulation; Direct Numerical Simulation (DNS), Large Eddy Simulation (LES) or Reynolds Averaged Navier Stokes (RANS), impacts how turbulence will be modelled due to their respective resolution levels. DNS simulations are the most resolved type of simulation, requiring a fine mesh, smaller than the Kolmogrov length scale to capture the entire turbulent spectrum. These types of simulations require tremendous computational resources; because of this these simulations are typically used when trying to understand the fundamental mechanism of turbulence within a given situation (Versteeg and Malalasekera, 2007). LES simulations resolve the large-scale turbulent structures, but the smaller scales are modelled. As a result, it requires less computational resources compared DNS while maintaining a relatively high degree of accuracy (Moukalled et al., 2016). Finally, RANS modelling is the least computationally expensive method, where the turbulence effects are entirely modelled by solving for the unknown Reynolds stress term. It is important to note that with RANS modelling, the flow properties (e.g. velocity, pressure, and stresses) are time averaged (Pope, 2020). Figure 1.3, offers a visual comparison of the various types of turbulence modelling.

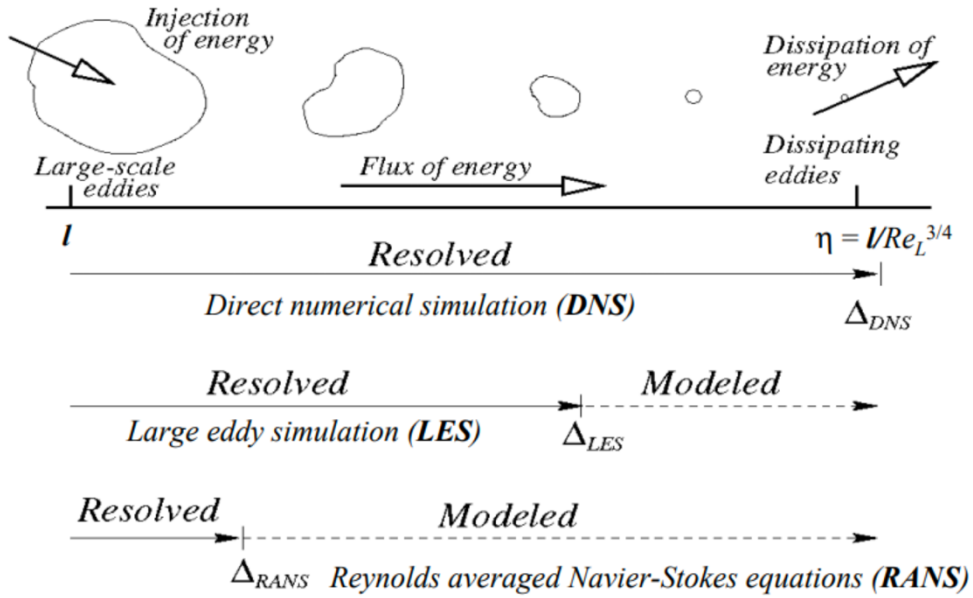

Figure 1.3: Comparison of DNS LES and RANS Modelling (Totten, 2019).

RANS turbulence modeling is based on the idea of separating the flow variables into mean and fluctuating components. In RANS simulations, the flow variables are decomposed into time-averaged quantities (mean flow) and fluctuating quantities (turbulent fluctuations). The time averaging process effectively filters out the high-frequency turbulent fluctuations, leaving behind a steady or time-averaged representation of the flow.

The $k-\varepsilon$ turbulence model is widely utilized due to its simplicity and effectiveness, solving two equations—one for turbulent kinetic energy, k and another for turbulent dissipation rate, ε (Launder and Spalding, 1974). While it excels in accurately predicting fully turbulent shear flows, it struggles with reliability in the near-wall region, a crucial area for many engineering applications (Menter, 2009).

On the other hand, the $k-\omega$ Wilcox model, also solving two equations for k and ω, offers improved reliability near walls compared to $k-\varepsilon$ (Launder, 1995). However, its dependency on

the ω term in the free stream poses a challenge, as obtaining an actual value for ω can be difficult (Menter, 1994).

The $k-\omega$ Shear Stress Transport (SST) model emerges as a balanced choice for this thesis, combining the strengths of both the $k-\varepsilon$ and $k-\omega$ Wilcox models. This method introduces a blending function that dynamically adjusts based on the distance from the wall, effectively incorporating $k-\varepsilon$ in the free stream and $k-\omega$ in the near-wall region. This approach optimizes accuracy across a (Menter et al., 2003).

Bubble-induced turbulence (BIT) serves a crucial role in extending the applicability of single-phase turbulence models to multiphase flow simulations (Lopez de Bertodano et al., 1994). In these simulations, BIT significantly influences the lateral distribution of bubbles within the flow field (Magolan et al., 2019). To incorporate BIT into turbulence models, source terms are introduced to account for the production and dissipation of bubble-induced turbulence (Rzehak and Krepper, 2013).

Various models exist for representing BIT, each employing different approaches to define key parameters such as the characteristic time scale, modulation parameter, and dissipation coefficient (Lahey, 2005) (Politano et al., 2003) (Troshko and Hassan, 2001). Among these models, the Ma model was selected for its applicability in contaminated systems and its suitability for small bubble sizes.

It's noted that the Ma model has primarily been tested on dilute gas holdups. According to the Ma model, the characteristic time scale is determined by the bubble diameter divided by the relative velocity. Additionally, the dissipation coefficient is a function of the drag coefficient, and the modulation parameter varies as a function of Reynolds number (Ma et al., 2017).

The main reasons for selecting the Ma model include its validity in contaminated systems, its applicability to small bubble sizes, and its adoption as part of the baseline model in the solver addon package. This comprehensive approach ensures that the chosen turbulence model accurately captures the effects of bubble-induced turbulence in multiphase flow simulations.

1.3.2 Drag Model Selection

Accurately predicting drag is paramount in the study of gas-liquid separation processes, as it profoundly influences phase velocities and phase distribution within the system (Tas-Koehler et al., 2021). A key challenge lies in developing drag models capable of handling the complex interactions between gas bubbles and the surrounding liquid medium. Traditionally, drag models have been formulated for scenarios involving a single bubble rising in a liquid, overlooking the complexities of multiphase flows with varying bubble sizes and distributions (Schiller and Naumann, 1934).

To address this limitation, researchers prioritize selecting drag models that are valid across a range of bubble regimes, allowing for easy extension and comparison to polydisperse data (Ishii and Zuber, 1979). Such models must capture phenomena like bubble deformation and interaction effects accurately. Among the available options, the Tomiyama drag model stands out for its comprehensive approach, accounting for bubble deformation and other intricate dynamics (Tomiyama et al., 1998).

Despite being developed for a single bubble in an infinite medium, (Lane et al., 2016b) experimentally observed that the Tomiyama drag model does not require a swarm correction at higher gas holdups in polydispersed bubbly flow. Typically, the rise velocity of a single bubble in an infinite medium is greater than that of a bubble in the presence of other bubbles due to the secondary flow fields imposed by neighboring bubbles. When validating the drag models against experimental data, they noticed a discrepancy between the gas holdup measured by a differential pressure sensor and the calculated holdup based off the optical probe measurements, this suggest the presence of many bubbles too small for the optical probe to measure (Mach et al., 2020b). They proposed that the presence of these small bubbles dampened the secondary flow fields, which ultimately reduced to the drag, such that it was appropriate to use a single isolated bubble uncorrected drag model.

1.4 Objectives

- Select appropriate turbulence and drag models capable of accurately capturing phase inversion phenomena and capable of being extended to inhomogeneous multiple size group

Population Balance Model (PBM), ensuring fidelity in simulating complex multiphase flows for accurate prediction of separation efficiency.

- Investigate the influence of key parameters, including bubble size, inlet gas phase fraction, liquid momentum, viscosity, and liquid recycle ratio, on the gas-liquid separation efficiency in multiphase CFD simulations.
- Explore the relationship between mean liquid residence time, gas holdup, and separation efficiency through comprehensive case studies, aiming to discern dominant factors affecting the separation process.
- Evaluate the significance of mean liquid residence time as a reliable predictor of separation efficiency, based on empirical observations and analysis from the conducted simulations.

Chapter 2

Numerical Methodology

2.1 Numerical Methods

OpenFOAM® is an open-source computational fluid dynamics software that uses the finite volume method (FVM) to solve the governing equations in multiphase flow simulations. FVM discretizes the computational domain into a "finite volumes" or cells, each surrounding a node on the mesh. The FVM is a popular approach to discretize and solve partial differential equations, other alternatives include the finite element method (FEM) and the finite difference method (FDM). The FVM offers the advantage of inherently conserving properties, a natural choice for fluid flow problems. In additional it offers the advantage of being highly adaptable for complex geometries and unstructured grid, due the versatility of the shape of the cells.

The FVM uses the Gaussian theorem to calculate the flux across each cell. The Gaussian theorem states the integral of the divergence of a given vector, over a closed volume, is equal to the flux of the same vector across the bounding surface, expressed mathematically in Equation (2.1)

.

$$\oint(\Delta \cdot \vec{\boldsymbol{a}})\, \boldsymbol{dV} = \oint \vec{\boldsymbol{a}} \cdot \hat{\boldsymbol{n}}\, \boldsymbol{dS} \tag{2.1}$$

The FVM uses this theorem to discretize partial differential equations (PDEs) over the computational domain. When the computational domain is discretized into finite volumes, the volume integrals of quantities such as mass flow and momentum flux can be converted into surface integrals. With this method conserved quantities can be calculated across boundary faces from cell centered values.

2.1.1 Governing Equations

In this section the mass and momentum conservation equations are derived for Euler-Euler simulations (Drew and Passman, 1998) (Yeoh and Tu, 2010). The Eulerian simulation approach was selected based on computational resources and the size of the computational domain.

Eulerian simulations focus on a specific location through time, as a result the flow variables are a function of position and time. These simulations require less computational resources compared to the Lagrangian, or fluid parcel tracking simulations.

Assuming the flow is incompressible, the mass conservation equation above can be simplified to the following.

$$\frac{\partial \rho}{\partial t} + \nabla \cdot \rho \vec{U} = 0 \tag{2.2}$$

Where ρ, represents the density of the fluid, t, time and $\vec{U}$, the velocity vector. The above equation is written for a single-phase simulation, to extend the mass conservation equation to a multiphase simulation the phase and phase fraction need to be included, represented herein with the *j* subscript and α, respectively.

$$\frac{\partial (\alpha_j \rho_j)}{\partial t} + \nabla \cdot (\alpha_j \rho_j \vec{U_j}) = 0 \tag{2.3}$$

The momentum conservation equation is written as follows.

$$\frac{\partial}{\partial t}(\rho \vec{U}) + \nabla \cdot \rho \vec{U}\vec{U} = -\nabla \mathrm{p} + (\nabla \cdot \tau) + \rho g \tag{2.4}$$

Where g represents acceleration due to gravity, p represents the pressure and τ, the stress tensor. For a Newtonian fluid, the stress tensor can be calculated as follows.

$$\tau = \mu \left\{ \nabla \vec{U} + (\nabla \vec{U})^T \right\} - \frac{2}{3} \mu (\nabla \cdot \vec{U}) I \tag{2.5}$$

Where μ represents the viscosity, the T superscript represents the transpose and I represents the identity matrix. Substituting the stress tensor equation into the momentum conservation equation gives the following.

$$\frac{\partial}{\partial t}(\rho \vec{U}) + \nabla \cdot \rho \vec{U}\vec{U} = -\nabla \mathrm{p} + \nabla \cdot \mu \left\{ \nabla \vec{U} + (\nabla \vec{U})^T \right\} + \left(\nabla - \frac{2}{3} \mu (\nabla \cdot \vec{U}) \right) + \rho g \tag{2.6}$$

For incompressible flows $\nabla \cdot \vec{U} = 0$, after applying this assumption the equation above can be simplified.

$$\frac{\partial}{\partial t}(\rho \vec{U}) + \nabla \cdot \rho \vec{U}\vec{U} = -\nabla \mathrm{p} + \nabla \cdot \mu \left\{ \nabla \vec{U} + (\nabla \vec{U})^T \right\} + \rho g \tag{2.7}$$

Rewritten for multiphase instances, the same process is applied as is shown for the mass conservation (Jones and Launder, 1972). Note the inclusion of the interfacial forces term, $\vec{M}$.

$$\frac{\partial(\alpha_j \rho_j \overrightarrow{U_j})}{\partial t} + \nabla \cdot (\alpha_j \rho_j \overrightarrow{U_j}\overrightarrow{U_j}) = -\alpha_j \nabla \mathbf{p} + \nabla \cdot \left(\alpha_j \overrightarrow{\tau_j}\right) + \alpha_j \rho_j \vec{\mathbf{g}} + \vec{M}_j \tag{2.8}$$

2.1.2 Interfacial Forces

The interfacial forces term is critical in multiphase simulations, as it encapsulates the complex interactions that occur at phase boundaries, including drag, lift, and turbulent dispersion, which have a significant impact on the behavior of the fluid. Numerically it can be expressed as follows.

$$\vec{M} = F_D + F_L + F_{TD} + F_{WL} + F_{VM} \tag{2.9}$$

Drag accounts for the resistance to motion experienced by the bubble due to the liquid. The drag coefficient was calculated using the Tomiyama slightly contaminated model (Tomiyama et al., 1998). This model was selected since it is valid for contaminated systems and accounts for bubble deformation.

$$F_D = -\frac{3}{4} C_d \frac{\alpha_g \rho_l}{d_b} \left|\overrightarrow{U_g} - \overrightarrow{U_l}\right| \left(\overrightarrow{U_g} - \overrightarrow{U_l}\right) \tag{2.10}$$

$$C_d = max\left\{min\left[\frac{24}{Re_b}\left(1 + 015 Re_b^{0.687}\right), \frac{72}{Re_b}\right], \frac{8}{3}\frac{Eo_b}{Eo_b + 4}\right\} \tag{2.11}$$

where Re_b and Eo_b represent the dispersed phase Reynolds and Eötvös numbers, respectively.

The lift force accounts for the lateral spread of bubbles and is calculated using the following equation.

$$F_L = -C_L \alpha_g \rho_l \left(\overrightarrow{U_g} - \overrightarrow{U_l}\right) \times \left(\nabla \times \overrightarrow{U_l}\right) \tag{2.12}$$

where C_L is the lift coefficient, which can be calculated using Tomiyama model (Tomiyama et al., 1998).

$$C_L = \begin{cases} \min\left[0.288 \tanh(0.121 Re,), f(Eo_{d,m})\right] & Eo_{d,m} < 4 \\ f(Eo_m) & 4 < Eo_{d,m} < 10 \\ -0.27 & 10 < Eo_{d,m} \end{cases} \tag{2.13}$$

where $Eo_{d,m}$ is a modified Eötvös number calculated on a horizontal bubble dimension instead of a Sauter mean bubble diameter (Wellek et al., 1966).

The turbulent dispersion forces account for spreading of the gas phase due to turbulent fluctuations. (Burns et al., 2004) introduced a Favre averaging technique, based on the drag coefficient, where σ_{TD} assumes a value of 0.9.

$$F_{TD} = -\frac{3}{4} C_d \frac{\alpha_g}{d_b} \left|\overrightarrow{U_g} - \overrightarrow{U_l}\right| \frac{\mu_{turb}}{\sigma_{TD}} \left(\frac{\nabla \alpha_g}{\alpha_g} - \frac{\nabla \alpha_l}{\alpha_l}\right) \tag{2.14}$$

A virtual mass coefficient C_{VM} of 0.5, typical for rigid spheres, was adopted (Magolan et al., 2019).

$$F_{VM} = C_{VM} \alpha_g \rho_l \left(\frac{\mathrm{D}U_g}{Dt} - \frac{\mathrm{D}U_l}{Dt}\right) \tag{2.15}$$

Wall lubrication forces are not included in the model as they are less impactful in turbulent simulations and due to the large size of the domain.

2.1.3 Turbulence Modelling

As previously discussed, RANS turbulence modelling was selected on account of its computationally efficiency and the 2-equation $k-\omega$ SST model was selected, based on its applicability in the transitional regime. The governing equations for the mean flow are obtained by applying Reynolds averaging to the Navier-Stokes equations. This results in a set of equations that describe the time-averaged behavior of the flow, where the effects of turbulence are represented through additional terms, referred to as Reynolds stresses, $\boldsymbol{R}$, see equation (**2.16** (Behzadi et al., 2004).

$$\boldsymbol{R} = -\rho \overline{U' U'} \tag{2.16}$$

The time averaging process effectively filters out the high-frequency turbulent fluctuations, leaving behind a steady or time-averaged representation of the flow. In Reynolds averaging the flow variables, such as velocity, pressure and viscosity are decomposed into a mean component, indicated by the overbar, $\bar{\phi}$ and a fluctuating component, indicated by the prime, ϕ'. See the equation below for a generalized mathematical expression of Reynolds averaged flow variables (Versteeg and Malalasekera, 2007).

$$\phi = \bar{\phi} + \phi' \tag{2.17}$$

The impact of Reynolds averaging on the mass and momentum conservation equations are as follows.

$$\frac{\partial \rho}{\partial t} + \nabla \cdot \rho \bar{U} = 0 \tag{2.18}$$

$$\frac{\partial}{\partial t}(\rho \bar{U}) + \nabla \cdot \rho \bar{U} \bar{U} = -\nabla \bar{\mathrm{p}} + \nabla \cdot \bar{\tau} + \rho g - \nabla \cdot \rho \overline{U'U'} \tag{2.19}$$

Where the instantaneous values were replaced with time averaged values such as $\vec{U}$, replaced with $\bar{U}$**,** p with $\bar{\mathrm{p}}$, τ with $\bar{\tau}$. Furthermore, the Reynolds stress term, $-\rho \overline{U'U'}$ was added.

The Boussineq eddy viscosity principle proposed that the Reynolds stress is proportional to the mean rates of deformation (Boussinesq, 1877). Recall Equation (**2.5**, which can be rewritten as follows to account for turbulent viscosity.

$$\tau = \mu_{turb} \left\{ \nabla \vec{U} + \left(\nabla \vec{U} \right)^T \right\} - \frac{2}{3} \left[\rho k + \mu_{turb} \left(\nabla \cdot \vec{U} \right) \right] I \tag{2.20}$$

Equation (**2.20** can be simplified under the incompressible flow assumption.

$$\tau = \mu_{turb} \left\{ \nabla \vec{U} + \left(\nabla \vec{U} \right)^T \right\} - \frac{2}{3} \rho k I \tag{2.21}$$

Where μ_{turb} represents the turbulent eddy viscosity and k represents the turbulent kinetic energy which is defined as follows.

$$k = \frac{1}{2} \vec{U} \cdot \vec{U} \tag{2.22}$$

Different types of turbulence models have been developed, which suggest alternative methods to solve for μ_{turb} which can be defined as follows.

$$\mu_{turb} = \rho l \sqrt{k} \tag{2.23}$$

To close the system of equations, turbulence models are introduced to provide closure for the Reynolds stresses. These models are based on physical principles and empirical correlations and aim to provide an approximate representation of the effects of turbulence on the mean flow. The most used turbulence model in RANS simulations is the k - ε and k - ω model, which solves transport equations for turbulent kinetic energy k and either its dissipation rate ε or the rate of dissipation of turbulent kinetic energy, ω. In this method 2 additional transport equations are

solved to account for effects like the convection and diffusion of turbulent kinetic energy. Both of these models have been derived for single phase flow, however they can be extended to multiphase flow by accounting for bubble induced turbulence (BIT) (Behzadi et al., 2004). Additionally due to the discrepancy in the density between the gas and liquid phase, the turbulence models need only be applied to the liquid phase since the turbulent effects in this phase will be significantly more pronounced than the gaseous phase.

The $k-\omega$ SST model was selected as the turbulence model for the liquid phase due to its applicability in a low Reynolds number regime and the reduced dependency on freestream ω values (Menter, 2009). The $k-\omega$ SST model solves 2 partial differential equations.

$$\frac{\partial \alpha_l \rho_l k}{\partial t} = \prod_k^{RANS} + D_k^{RANS} - C_\mu \alpha_l \rho_l \omega k + C_I F_D \left|\overrightarrow{U_g} - \overrightarrow{U_l}\right| \tag{2.24}$$

$$\frac{\partial \alpha_l \rho_l \omega}{\partial t} = \prod_\omega^{RANS} + D_\omega^{RANS} + C_\omega^{RANS} - C_{\omega D} \alpha_l \rho_l \omega^2 + \left(\frac{1}{C_\mu k} S_\varepsilon^{RANS} - \frac{\omega}{k} S_k^{RANS}\right) \tag{2.25}$$

Where Π_k^{RANS} is the production term and D_k^{RANS} is the dissipation term, both of which are the same as with single phase flow (Menter, 1994). The final term in both equations above represent the BIT source term (Ma et al., 2017). BIT refers to the turbulent fluctuations generated by by the motion and interaction of gas bubbles within a liquid phase in multiphase flows. More specifically BIT can have a significant impact on the lateral phase distribution, and therefore the lift force. In systems where gas-liquid interactions occur, such as bubbly flows or gas-liquid reactors, the presence of bubbles can significantly alter the flow dynamics, leading to enhanced turbulence levels compared to single-phase flows. BIT for the 2 equation turbulence models is typically accounted for by including additional source terms to the turbulent transport equations. The Ma model was selected on account of its applicability for smaller bubbles in contaminated systems. Additionally, the closure uses easily accessible and widely used parameters such as Re_b and C_d. Furthermore, it is a part of the `HZDRmutltiphaseEulerFoam` solver's baseline model.

$$S_k^{RANS} = \min\left(0.18 Re_b^{0.23}, 1\right) F_D\left(\overrightarrow{U_g} - \overrightarrow{U_l}\right) \tag{2.26}$$

$$S_\varepsilon^{RANS} = C_\varepsilon \frac{S_k^{RANS}}{t_{char}} \tag{2.27}$$

$$t_{char}\ \frac{d_b}{|\overrightarrow{U_g}-\overrightarrow{U_l}|} \tag{2.28}$$

$$C_\mu = 0.09 \tag{2.29}$$

$$C_I = \min\left(0.18Re_b^{0.23}, 1\right) \tag{2.30}$$

$$C_\omega^{RANS} = (1-F_1)2\rho\sigma_{\omega 2}\frac{1}{\omega}\frac{\partial k}{\partial x_j}\frac{\partial \omega}{\partial x_j} \tag{2.31}$$

$$C_{\omega D} = 0.0828 \tag{2.32}$$

$$C_\varepsilon = 0.3C_D \tag{2.33}$$

$$C_L = 0.06 \tag{2.34}$$

2.1.4 Solver Algorithm

The `HZDRmultiphaseEulerFoam` solver, developed by (Schlegel et al., 2022), served as the primary algorithm for conducting all simulations in this study. This specialized solver was chosen due to its comprehensive suite of models tailored specifically for multiphase flow simulations. Its inclusion of key pieces of work such as (Rzehak and Krepper, 2013), (Liao et al., 2019), and (Liao et al., 2018) and (Ma et al., 2017) held significant relevance to the objectives of this research.

The `HZDRmultiphaseEulerFoam` solver employs the PIMPLE algorithm to solve the governing equations. The PIMPLE algorithm represents a fusion of the Semi-Implicit Method for Pressure-Linked Equations (SIMPLE) and the Pressure Implicit with Splitting of Operators (PISO) algorithms. While the PISO algorithm extends the capabilities of SIMPLE to transient state simulations, it is subject to strict time stepping limitations imposed by the Courant Number remaining less than 1. By combining these two methods, the PIMPLE algorithm leverages the inner PISO loop for transient problems and the outer SIMPLE loop for larger time stepping, thereby enhancing its versatility and efficiency in handling unsteady state flow scenarios.

A comparison of the SIMPLE and PISO algorithms can be seen in Figure 2.1. Both SIMPLE and PISO have similar initialization and predictor steps, however the SIMPLE algorithm uses the momentum equations to solve for the velocity. The velocity field is then calculated without the

contributions of the pressure gradient. Then the pressure equation is solved and finally the velocity is corrected using the pressure gradient.

In contrast the PISO algorithm adds an intermediate velocity correction using an intermediate pressure field, in essence repeating steps 2-6 in Figure 2.1, before proceeding in time. This correction ensures a divergence free velocity, and time accurate results. One benefit of this scheme is its inherent stability owing to the additional steps taken to achieve a divergence free velocity. Unfortunately for the same reason this algorithm is also computationally more expensive when compared to the SIMPLE algorithm.

In Figure 2.1, a straightforward comparison of the two individual algorithms, SIMPLE and PISO, is presented. This comparison outlines the basic steps involved in each algorithm's solution process, offering a clear overview of their respective approaches to solving the governing equations of the fluid flow problem. Each step is succinctly depicted, providing a concise understanding of the fundamental procedures employed by each algorithm.

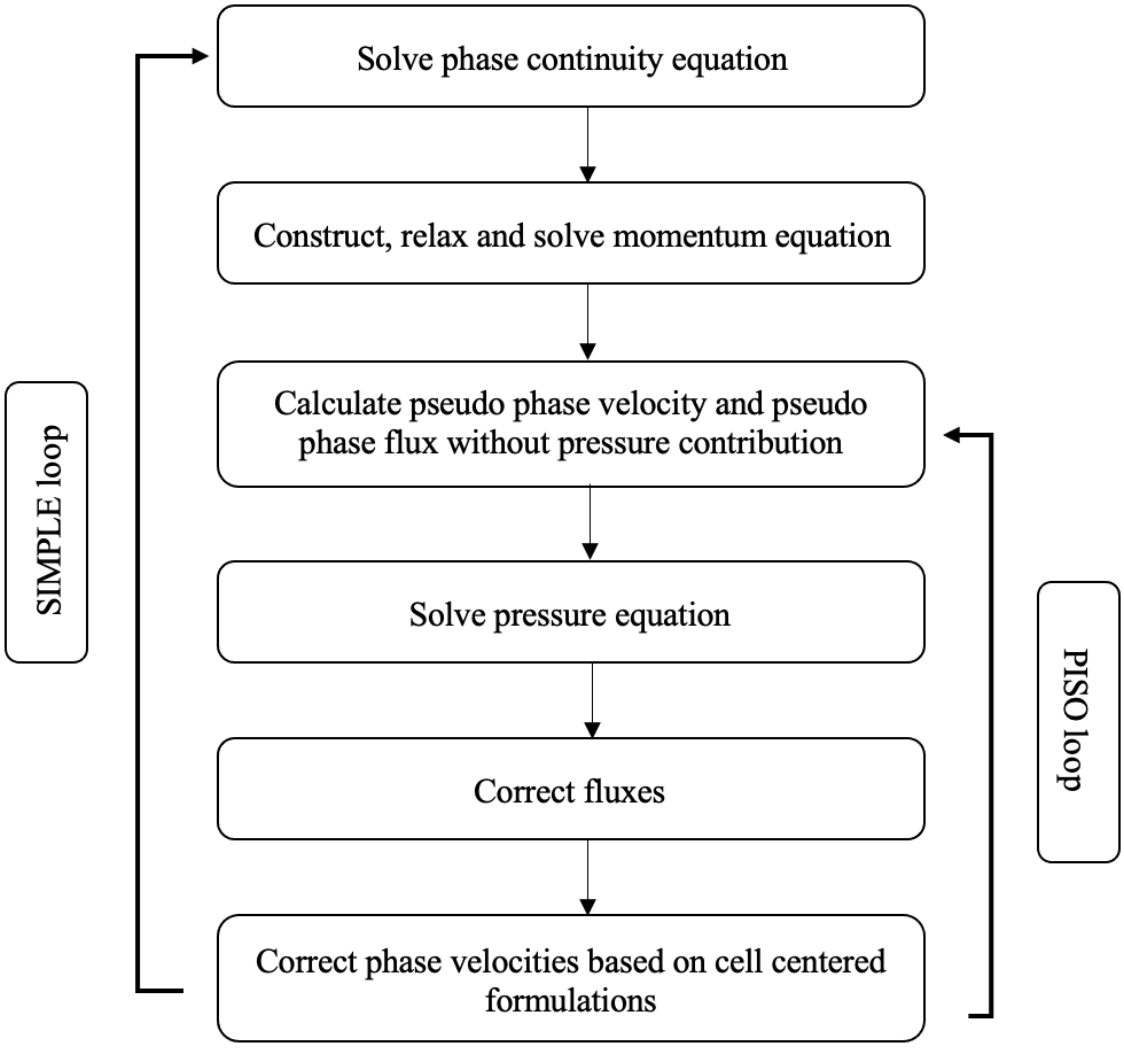

Figure 2.1: Comparison of SIMPLE and PISO Algorithm

On the other hand, Figure 2.2 provides a more detailed look at the PIMPLE algorithm, offering insight into the full extent of the solution process. This detailed depiction delves into the intricacies of the algorithm, highlighting not only the primary steps involved but also incorporating additional elements such as time steps, convergence checks, and iterative procedures.

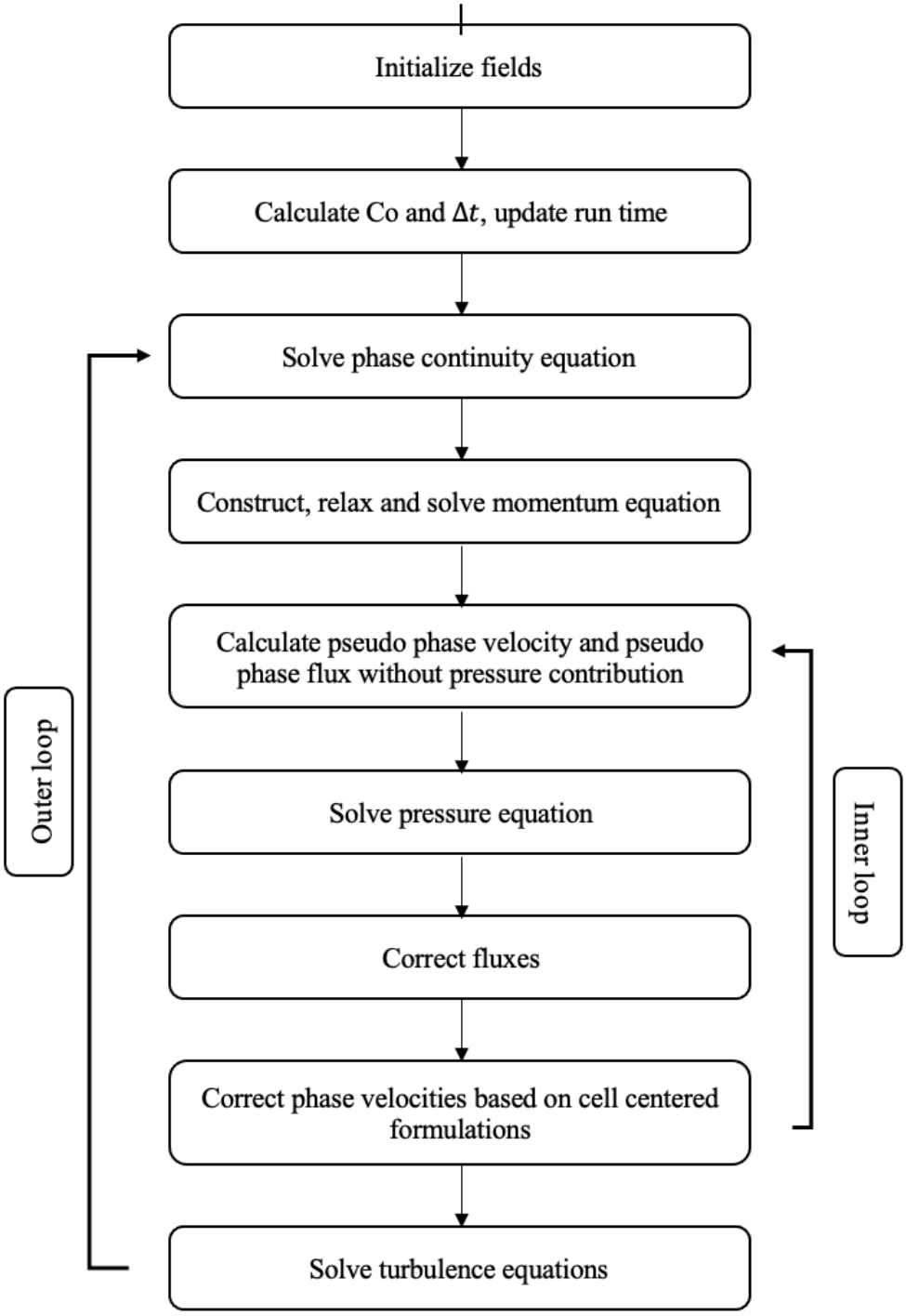

Figure 2.2: PIMPLE Algorithm

2.1.5 Discretization Scheme Selection

The selection of finite volume schemes in this study is underpinned by a thoughtful consideration of accuracy, stability, and computational efficiency, see Table 2.1. For temporal discretization, a first-order scheme was chosen as the primary objective was to achieve pseudo-steady-state results. This approach balances computational efficiency and robustness, facilitating convergence to the desired pseudo-steady state solution.

Table 2.1: Finite Volume Schemes

Term	Scheme
Time Discretization	Euler
Gradient Discretization	Gauss Linear
Laplacian Discretization	Gauss Linear Corrected
Face Interpolation	Linear
Surface Normal Gradient Discretization	Corrected

A summary of the numerical schemes for the convective terms can be found in Table 2.2. A second-order upwind-weighted spatial discretization scheme was selected based on its numerical stability and accuracy. The upwind weighting captures the dominant flow directions, curbing the onset of numerical oscillations and ensuring robust stability in simulations (Versteeg and Malalasekera, 2007).

Table 2.2: Convective Schemes

Term	Scheme
$\nabla \cdot \phi\alpha$	Gauss Linear Upwind
$\nabla \cdot \alpha\rho\phi U$	Gauss Linear Upwind
$\nabla \cdot \phi U$	Gauss Linear Upwind
$\nabla \cdot \alpha\rho\phi k$	Gauss Linear Upwind
$\nabla \cdot \alpha\rho\phi\varepsilon$	Gauss Linear Upwind
$\nabla \cdot \alpha\rho\phi\omega$	Gauss Linear Upwind
$\nabla \cdot \alpha\phi f$	Gauss Linear Upwind
$\nabla \cdot \upsilon_{eff}$	Gauss Linear

A summary of the solvers and tolerances are shown in Table 2.3. This information outlines the convergence criteria and numerical methods used in the solution process for key variables.

Table 2.3: Solvers and Tolerance

Variable	Solver	Smoother	Tolerance

$\boldsymbol{p_{rgh}}$	GAMG	Diagonal-based Incomplete Cholesky	1×10^{-6}
U	Smooth	Symmetric Gauss Seidel	1×10^{-5}
$k\|\varepsilon\|\omega$	Smooth	Symmetric Gauss Seidel	1×10^{-7}

2.2 Model Preparation

A 90-degree wedge configuration was employed to replicate the geometry of an EBHR pilot plant. This arrangement comprised two pipes, each equipped with a 90-degree elbow. The inlet conditions were replicated using the two pipe intakes, as shown in Figure 2.3 the system featured two outlets: one for recycle, and another for the product line. The length of the modelled recycle line was determined to be 10 times larger than the diameter. The overall control volume is approximately 0.38m^3.

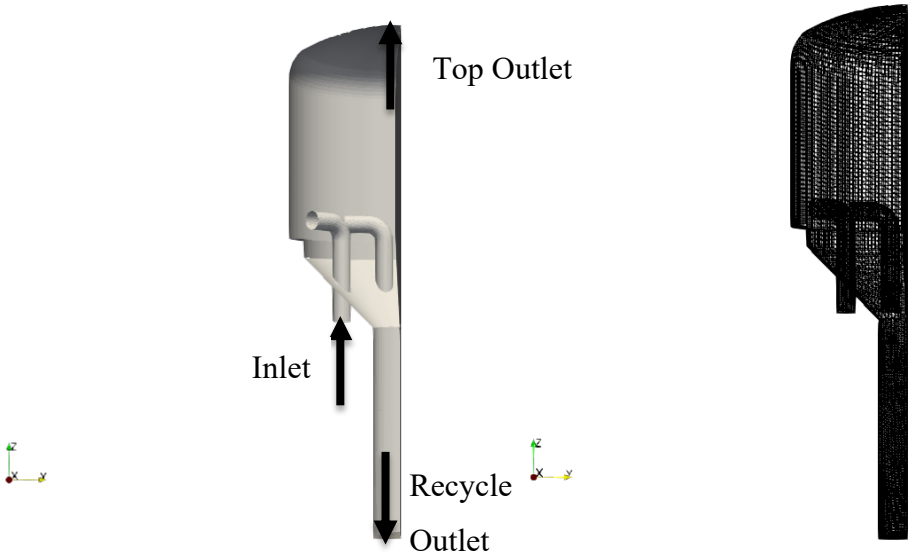

Figure 2.3: CAD and Meshed Control Volume

2.2.1 Boundary Conditions

Table 2.4 summarizes the boundary conditions applied to the walls, inlets and outlets. A `zeroGradient` boundary condition can be represented mathematically as follows.

$$\frac{\partial \phi}{\partial n} = 0 \tag{2.35}$$

Where ϕ is the variable of interest and n is the direction normal to the boundary. This boundary for both `alpha.air` and `alpha.water` imposed along the wall indicates an impenetrable surface. When imposed at the top outlet for both phase fractions it acts as a flexible boundary condition, allowing the phase to exit the domain, based on the flow field. The `inletOutlet` boundary condition is imposed at the recycle outlet since it allows for backflow, which occurs due to the geometry, ultimately this boundary is required to stabilize the simulation.

The velocity boundary conditions imposed along the walls for the gas phase is `slip`, while the liquid uses a `noSlip` boundary condition. The recycle outlet for air is a custom boundary condition, it is defined as the summation of slip and the liquid. Here slip is defined as the difference between the air and water velocity. For both gas and liquid, the top outlet is defined as `pressureInletOutletParSlipVelocity`, this boundary acts as a `zeroGradient` boundary for outflow, however it can also act as inlet. The pressure indicates that the pressure field is being set at this boundary and ensures the system is not over constrained. The `prghTotalPressure` boundary condition was selected for the top outlet, which calculates the pressure as follows, here the liquid velocity is used in the calculation of static pressure.

$$p_r gh = p - \rho g(h - h_{ref}) \tag{2.36}$$

$$p = p0 - 0.5\rho|U|^2 \tag{2.37}$$

.

Table 2.4: OpenFOAM Boundary Conditions

	Inlet	Outlet Top	Outlet Recycle	Walls
alpha.air	fixedValue	zeroGradient	inletOutlet	zeroGradient
alpha.water	fixedValue	zeroGradient	inletOutlet	zeroGradient
U.air	fixedValue	pressureInletOutletParSlipVelocity	U.air = U.water+U.slip	slip
U.water	fixedValue	pressureInletOutletParSlipVelocity	flowRateOutletVelocity	noSlip
p_rgh	fixedFluxPressure	prghTotalPressure	zeroGradient	fixedFluxPressure
P	calculated	calculated	calculated	calculated
k	fixedValue	inletOutlet	inletOutlet	kqRWallFunction
omega	fixedValue	inletOutlet	inletOutlet	omegaWallFunction
T.air	fixedValue	zeroGradient	zeroGradient	zeroGradient
T.water	fixedValue	zeroGradient	zeroGradient	zeroGradient

2.3 Operating Conditions

Table 2.5 presents the simulation conditions for the parametric study. Each simulation used a single bubble diameter within the range of 0.3–1 mm. The velocity and phase fraction of both phases were set at the inlets (Lane et al., 2016a). The liquid recycle ratio, $\mathcal{R}$, is defined as the ratio of liquid that exits the computational domain through the recycle outlet over the total flow of liquid entering the domain.

$$\mathcal{R} = \frac{\dot{m}_{Recycle\ line}}{\dot{m}_{inlet}} \tag{2.38}$$

The liquid recycle ratio is physically controlled by the pump speed, but here is enforced through an imposed liquid mass flow rate boundary condition at the recycle outlet. Air and water at ambient conditions were selected for phase physical properties as there is more bubble coalescence and breakup data readily available for future inclusion of a population balance model.

The gas liquid separation efficiency is defined as follows (Lane et al., 2019b).

$$\eta = 1 - \frac{\dot{m}_{g,recycle}/\dot{m}_{g,column}}{\mathcal{R}} \tag{2.39}$$

where η is the separation efficiency, $\dot{m}_{g,recycle}$ is the mass flow rate of gas through the recycle line, and $\dot{m}_{g,column}$ is the mass flow rate of gas entering through the recycle pan pipe inlets. With this definition a separation efficiency of 0 indicates the gas-to-liquid ratio that exits through the recycle line boundary is equivalent to the gas-to-liquid ratio that enters the freeboard region. In contrast, a separation efficiency of 1 indicates that all the gas exits through the top outlet.

Table 2.5: Boundary Operating Conditions and Phase Physical Properties

Condition	Base Case	Range	Units
Inlet Liquid Volumetric Flow Rate	9.65×10^{-3}	$5.81 - 19.4 \times 10^{-3}$	$m^3\ s^{-1}$
Inlet Gas Volumetric Flow Rate	1.11×10^{-2}	$1.11 - 13.4 \times 10^{-3}$	$m^3\ s^{-1}$
Inlet Liquid Holdup	0.5	0.4-0.95	-
Inlet Gas Holdup	0.5	0.05-0.6	-
Liquid Recycle Ratio	0.8	0.5-0.9	-

Bubble Diameter	0.8	0.3-1	mm
Liquid Density	997	997	$kg\ m^{-3}$
Gas Density	1.184	1.184	$kg\ m^{-3}$
Liquid Viscosity	8.9×10^{-4}	$7.6 - 13.4 \times 10^{-4}$	Pa s
Gas Viscosity	1.85×10^{-5}	1.85×10^{-5}	Pa s
Surface Tension	0.072	0.072	$N\ m^{-1}$

2.4 Benchmarking Computational Framework

The selection of discretization schemes and solver selection were guided by baseline models as well as the need to achieve a stable solution. Some modifications to the baseline model were required to achieve convergence for the conditions studied in this work, as is detailed in Section 2.1.5. The impact of these results was studied through simplified cases, with a 2D structured mesh bubble column, the results can be seen in the Figures below. There are slight variations in the liquid flow field however the overall magnitude is very similar.

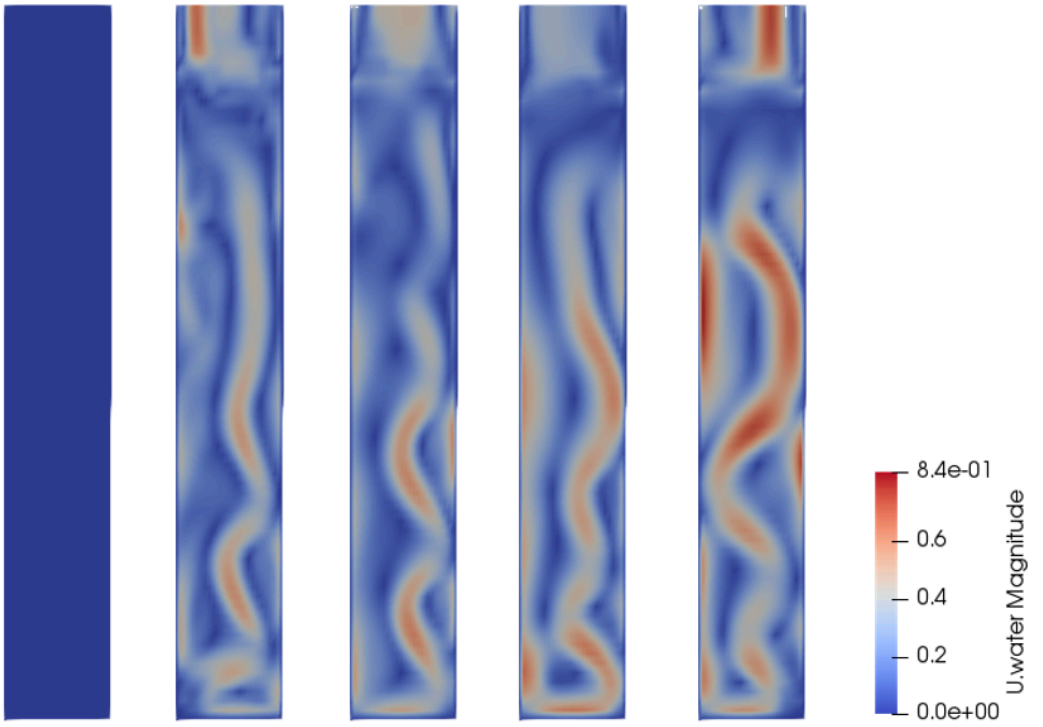

Figure 2.4: Baseline Bubble Column Model at (a) 0 s (b) 10 s (c) 20 s (d) 30 s (e) 40s.

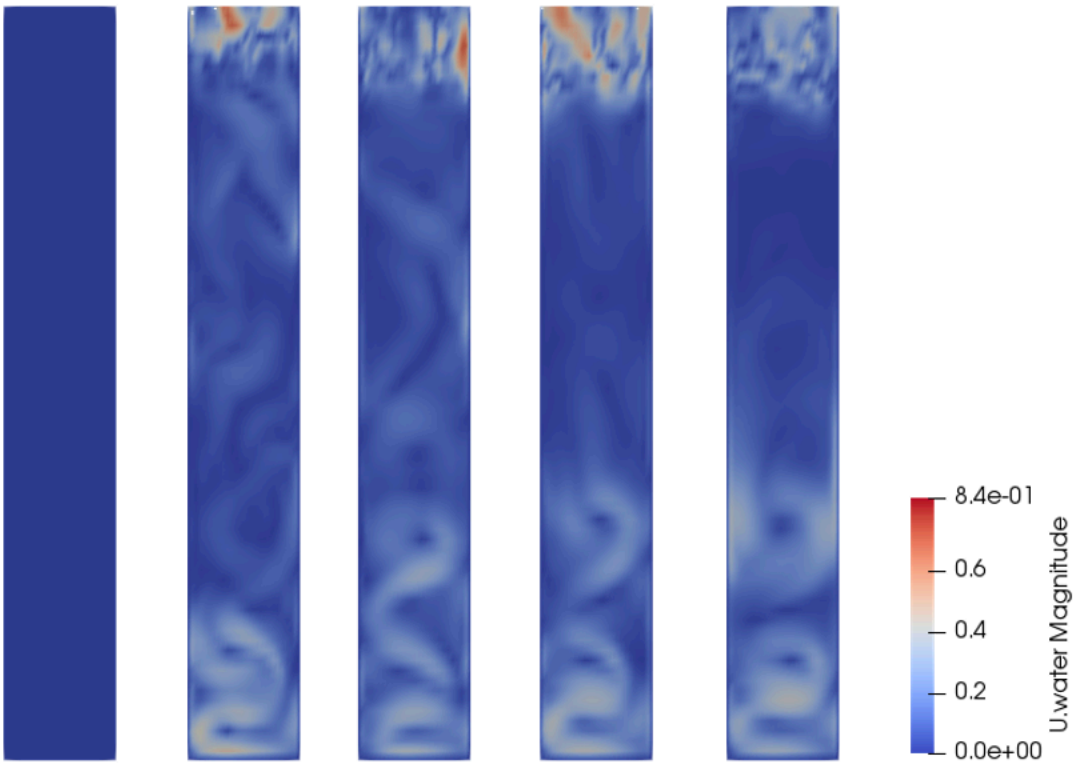

Figure 2.5: Modified Numerical Schemes Bubble Column Model at (a) 0 s (b) 10s (c) 20 s (d) 30 s (e) 40s.

After validating the numerical schemes on a simplified 2D geometry, a 3D control volume was constructed. A crucial design decision involved extending the recycle line so that its outlet was sufficiently far from the active separation region. This ensured that the boundary conditions at the recycle line outlet did not significantly influence the active separation region. Consequently, the recycle line's length was made ten times greater than its diameter to allow sufficient flow development and minimize entrance effects before applying the boundary conditions. Additionally increasing the length beyond this range had negligible impact on the flow field.

To ascertain an appropriate mesh resolution, a mesh dependence study was conducted. This involved calculating and plotting the gas holdup across the entire computational domain over time, as depicted in Figure 2.6. The results from all three mesh sizes demonstrated similar predictions, which indicates adequate mesh resolution. Ultimately, a mesh consisting of 120,000 cells was

selected. This choice was guided by the necessity to accurately capture key boundaries while maintaining a reasonable computational runtime.

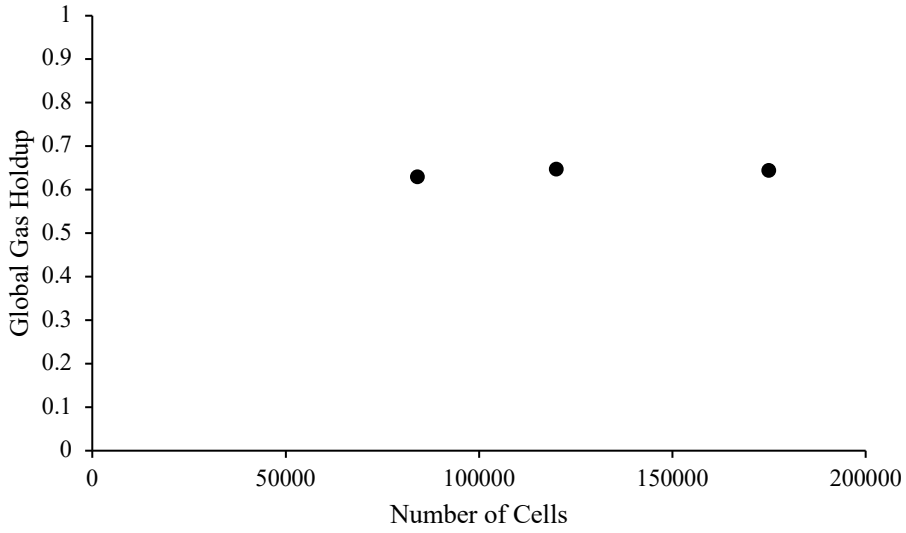

Figure 2.6: Gas Holdup at Pseudo-Steady State for Various Mesh Sizes.

Chapter 3

Results and Discussion

3.1 Single Phase

Single-phase simulations were conducted initially to validate mesh quality, assess the need for a turbulence model, and gain insights into flow dynamics. The liquid streamlines, shown in Figure 3.1, illustrate the deliberate impact of offset inlet pipe on the swirling flow pattern. Note the left- and right-hand side of Figure 3.1 are of the same simulated control volume but rotated by 90° along the z axis. The inlet pipe orientation induces a tangential flow, evident in the upward swirling streamlines observed. Ideally, the centrifugal force would cause a radial pressure gradient that would push the dense liquid phase to the exterior wall and concentrate the lighter phase in the center of the vessel, promoting bubble coalescence and then separation. Furthermore, this induced swirl increases mean liquid residence time, facilitating gas liquid separation (Lane et al., 2019b).

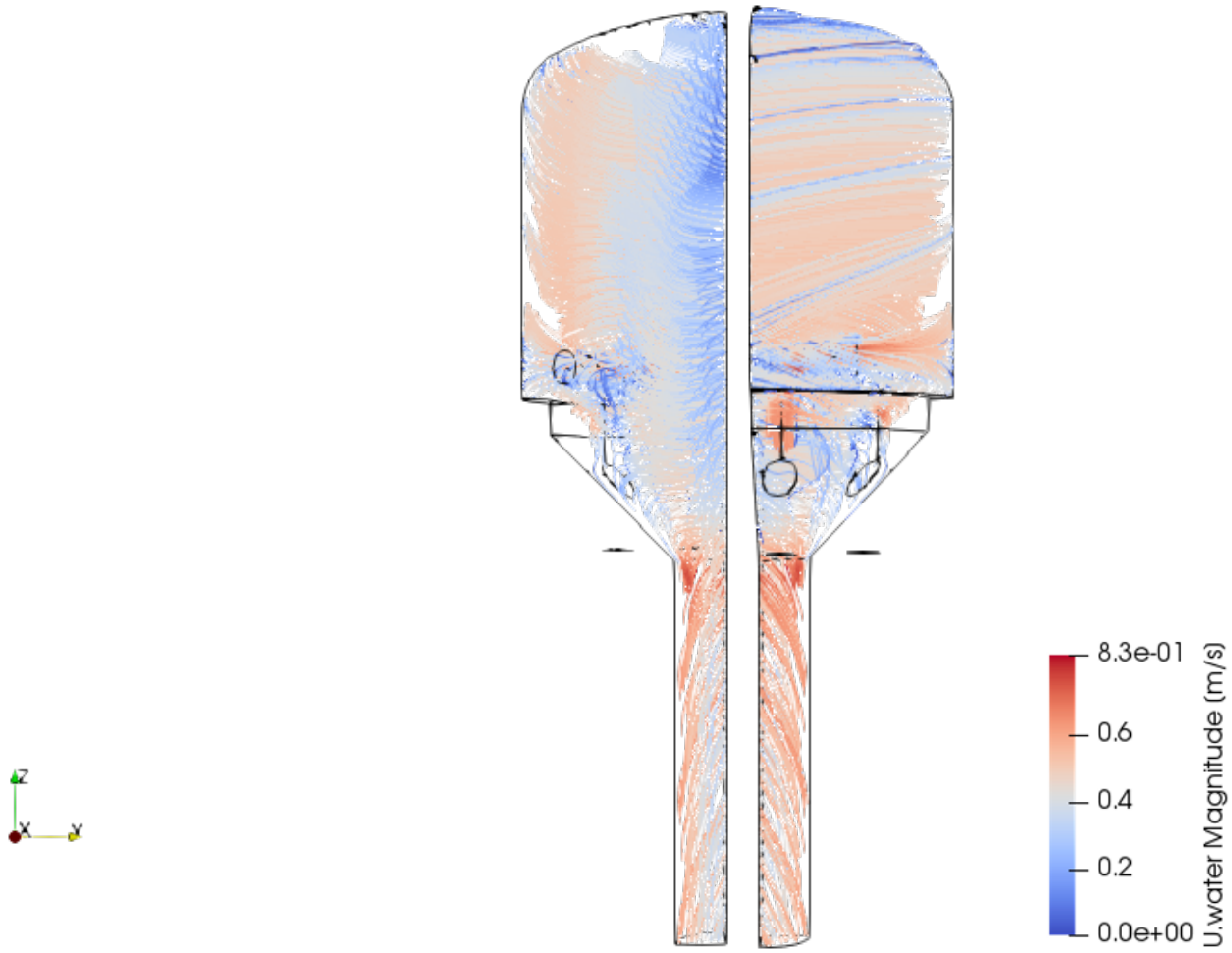

Figure 3.1: Single Phase Streamlines at 130s for Base Case Conditions Stated in Table 2.5. Right Hand Side Rotated by 90° Along the z Axis

Figure 3.2, compares the laminar and turbulent single-phase simulations. Throughout all studies turbulence was only included for the liquid phase since the liquid viscosity and density are much greater than the gas phase. Including the gaseous turbulence will have a negligible effect on the overall results and significantly increase the computational run time. When the Reynolds number enters the transitional regime, disturbances within the flow grow into vortices due to insufficient stabilizing frictional forces. The emergence of these time-dependent secondary flows, observable in the simulation results, underscores the necessity of turbulence modeling to accurately capture flow dynamics.

In the k- ω turbulence model, the turbulent viscosity, μ_t serves as a crucial modeled parameter derived from turbulent kinetic energy, k and specific dissipation rate, ω. It quantifies the additional momentum transport resulting from unresolved turbulent fluctuations, capturing the intricate effects of turbulent mixing and eddy diffusion. Through the solution of additional transport equations for k and ω, this model offers closure to the RANS equations. The turbulent viscosity, representing an averaged value within the flow domain, enables the model to approximate the impact of unresolved turbulence on the mean flow. Despite its utility, it does not fully encapsulate all scales of turbulence at every point in the domain, a limitation that contributes to the computational efficiency relative to DNS or LES.

In contrast, laminar simulations rely on a constant viscosity and do not incorporate turbulence modeling. When the Reynolds number enters transitional or turbulent regimes, disturbances within the flow grow into eddies and vortices due to insufficient stabilizing frictional forces. The emergence of these eddies, observable in the simulation results, underscores the necessity of turbulence modeling to accurately capture flow dynamics.

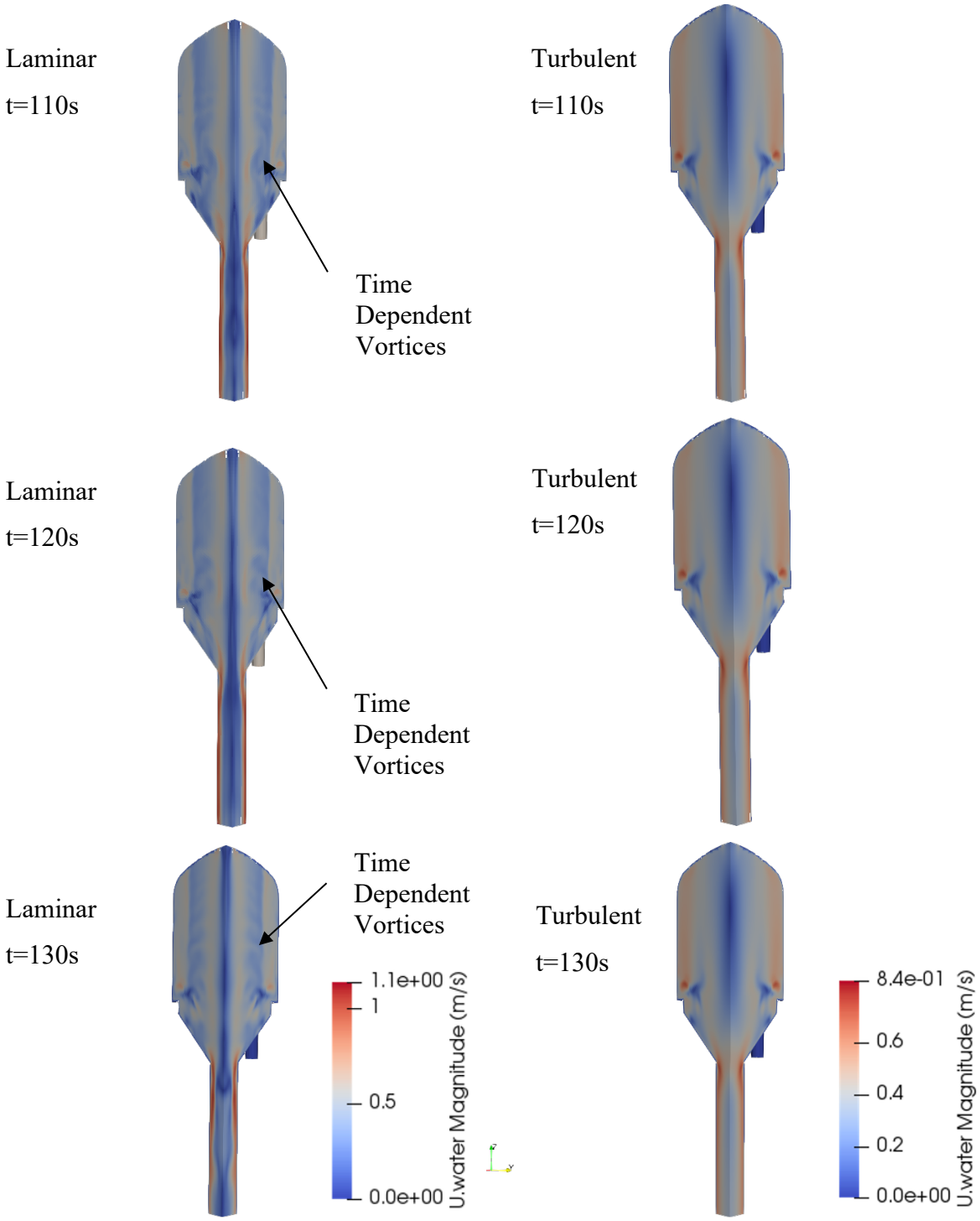

Figure 3.2: Liquid Velocity Profile and Time Dependent Vortices in Laminar vs Turbulent Flow. Liquid Phase Base Case Conditions in Table 2.5.

3.2 Multiphase Simulation

3.2.1 Achieving Pseudo-Steady State

Figure 3.3 shows the evolution of the global gas holdup from startup to pseudo-steady state. At startup the vessel is filled with liquid, as time increases three distinct regions begin to form. The gas rich region near the top of the vessel, shown in red, a conical section in the middle of the vessel, which is pale blue and a liquid-rich region in the bottom of the vessel. The gas-rich region expands as the global gas holdup increases, reducing the space available for the liquid phase. Therefore, the size of the gas-rich region has a direct impact on the mean liquid residence time defined below. Once the global gas holdup is constant and the mass balance on both phases close, the simulation is considered to have reached pseudo-steady state. The average percent difference for the species mass balance was 4.5% and 1.5% for the gas and liquid phases respectively, with a maximum difference of 18%.

$$Liquid\ Residence\ Time_{mean} = \frac{(1-\alpha_G)V}{Q_{l,inlet}} \tag{3.1}$$

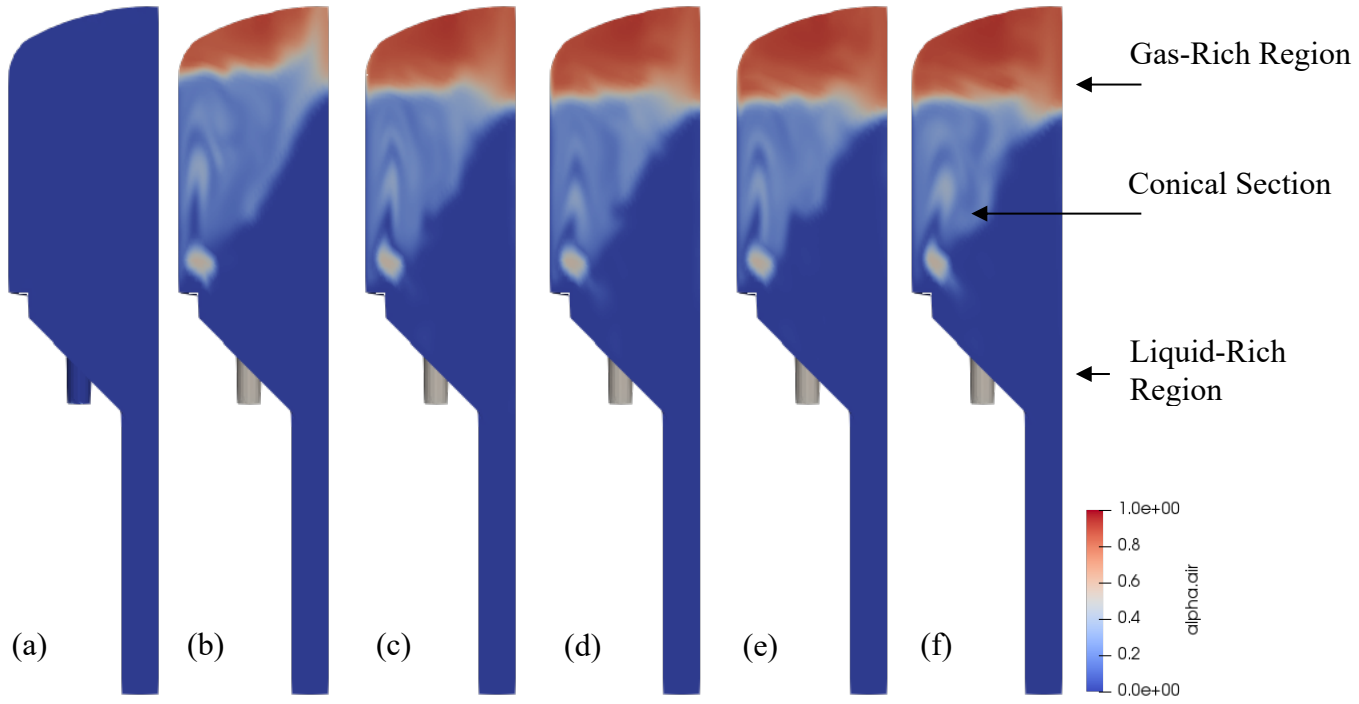

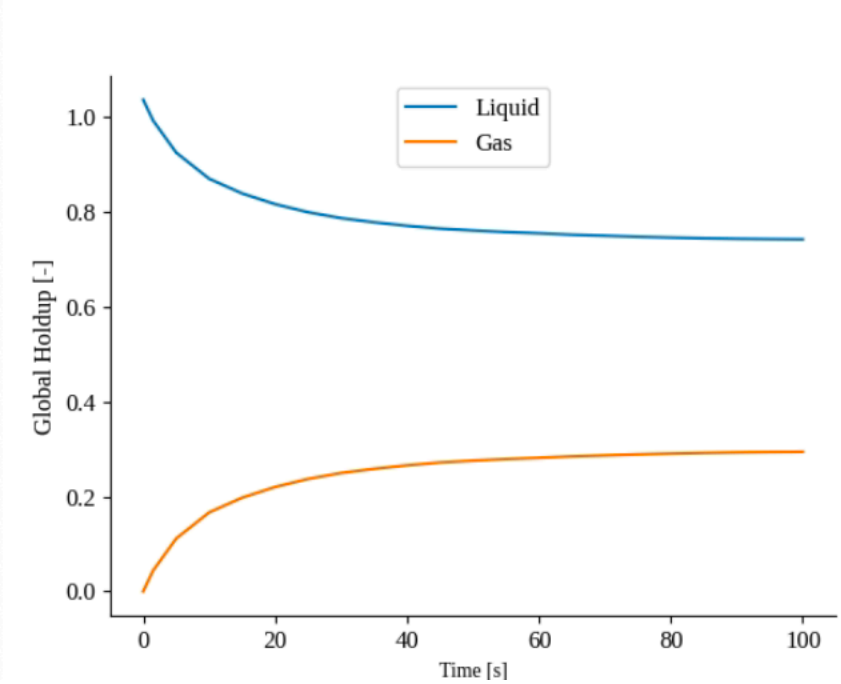

Figure 3.3: Global Gas Holdup for a 1 mm Bubble at Time (a) 0 s (b) 20s (c) 40 s (d) 60 s (e) 80 s (f) 100 s. All Other Parameters Under Base Case Conditions as per Table 2.5.

3.2.2 Bubble Size Case Study

Simulations with volume-equivalent sphere diameters ranging from 0.6–1 mm were performed under base case conditions to investigate the impact of bubble size on gas separation efficiency. The results shown in Table 3.1 indicate that larger bubbles separate more readily than smaller bubbles. From a simplified force balance, as the bubble diameter increases, the net gravity force based on bubble volume will increase faster than the drag force based on bubble surface area. This force imbalance allows the larger bubbles to rise faster, disengaging from liquid streamlines more readily.

Table 3.1: Key Parameters of Bubble Size Case Study. All Other Parameters Under Base Case Conditions as per Table 2.5.

Bubble Size [mm]	Mean Liquid Residence Time [s]	Global Gas Holdup [-]	Separation Efficiency [-]
0.60	15.75	0.60	0.03
0.70	17.84	0.55	0.11

0.80	24.02	0.39	1.00
1.00	29.14	0.26	1.00

Figure 3.4 shows the liquid streamlines of a separating and non-separating system. For the separating system the liquid follows the ideal streamlines, a swirl is induced, because of the offset elbowed pipe inlets causing a radial pressure gradient. This increases mean liquid residence time, promoting gas separation. For smaller bubble sizes, or more generally for non-separating systems, bubbles do not have a sufficiently large relative velocity to readily separate from the liquid streamlines. Instead, they more closely follow the liquid streamlines, taking an indirect path towards the top of vessel, occupying both more time and space inside the control volume. This phenomenon has a visible impact on the liquid streamlines. In non-separating systems the liquid streamlines exhibit strong axial recirculation zones compared to the induced swirl for separating systems.

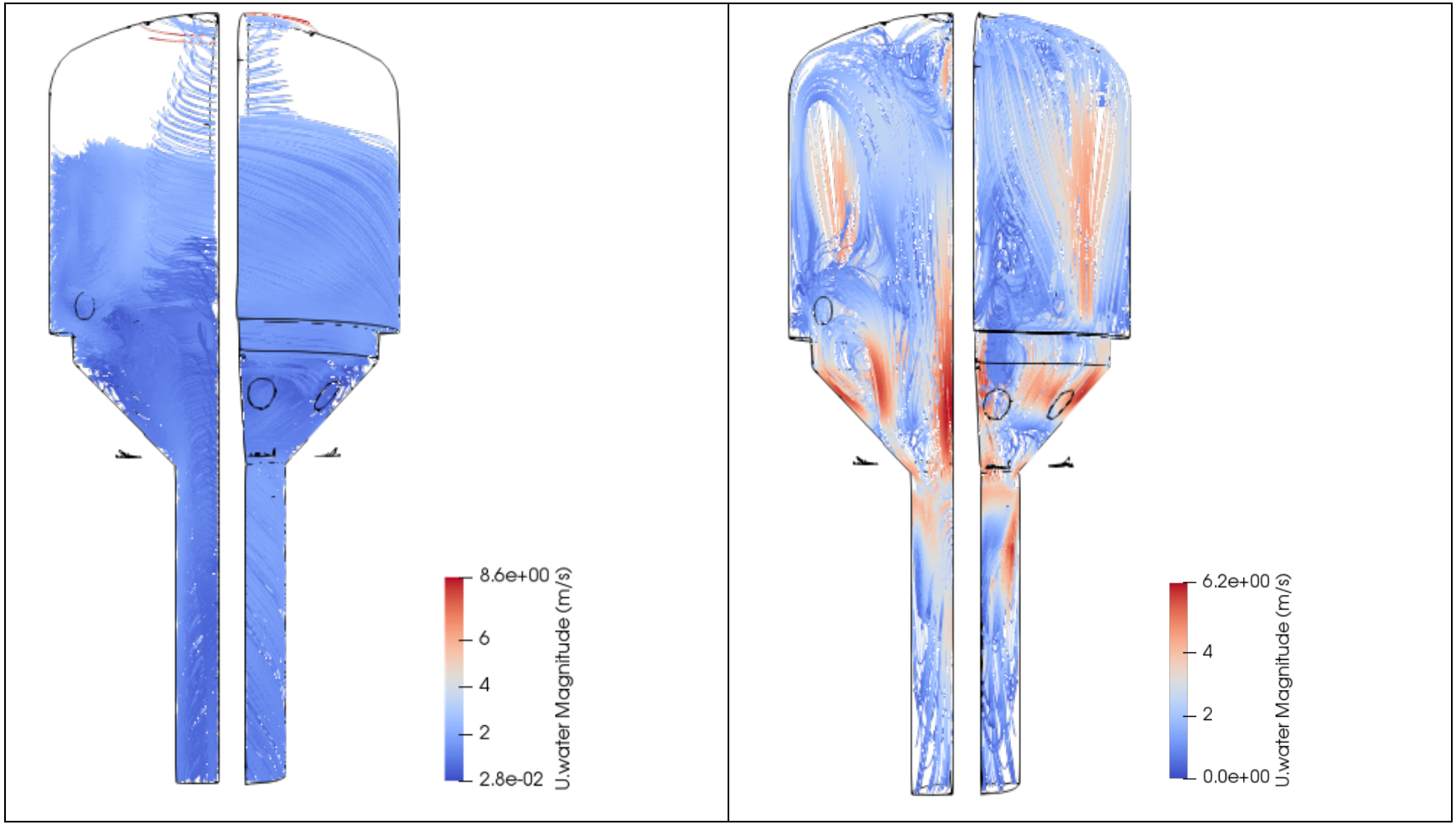

Figure 3.4: Liquid Streamlines for a) 0.8 mm Diameter Bubble with Visible Swirl at 150 seconds and (b) 0.6 mm Diameter Bubble with Visible Recirculation Zones at 90 seconds. All Other Parameters are at Base Case Conditions as per Table 2.5.

3.2.3 Inlet Gas Holdup Case Study

The inlet gas fraction is varied by changing the inlet gas flow rate while keeping all other parameters constant. The impact of inlet gas faction on separation efficiency for various sized bubbles is shown in Figure 3.5. As the inlet gas phase fraction increases, the global gas holdup rises which reduces the space available for the liquid to circulate, and ultimately the mean liquid residence time. As a result, smaller bubbles can be separated with a lower inlet gas phase fraction (e.g. a 0.6 mm diameter bubble will separate with an inlet gas holdup of 0.05 but not when the holdup rises to either 0.5 or 0.6). Increasing the mean liquid residence time naturally increases gas-liquid separation by allowing sufficient time for the bubbles to disengage from the liquid streamlines. Therefore, as the mean liquid residence time increases so does the separation efficiency.

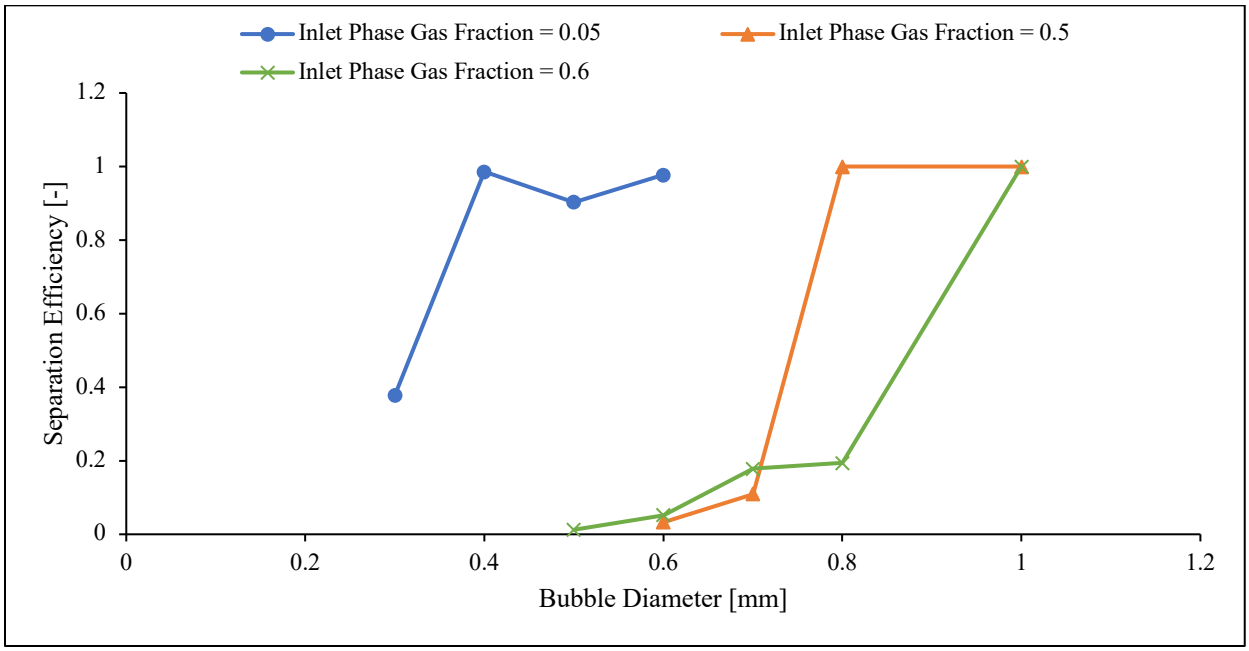

Figure 3.5: Separation Efficiency for Various Bubble Sizes at Increasing Inlet Gas Fractions. All Other Parameters are at Base Case Conditions as per Table 2.5.

3.2.4 Liquid Momentum

The effects of liquid momentum (which encompasses both the liquid flow rate and the gas-to-liquid ratio) on separation efficiency are summarized in Table 3.2. Interestingly all the simulated conditions have a separation efficiency near 100%, likely owing to competing factors both facilitating and hindering gas-liquid separation. As the liquid momentum increases a stronger centrifugal force is observed, which promotes separation efficiency. However based on the increased liquid flow rate entering the vessel, the draw from the recycle line is increased, making it more difficult for bubbles to separate. In addition, increasing the liquid flow rate entering the vessel reduces the mean liquid residence time.

Table 3.2: Impact of Inlet Liquid Momentum on Flow Field and Separation Efficiency All Other Parameters Under Base Case Conditions as per Table 2.5.

Bubble Size [mm]	Inlet Liquid Volumetric Flow Rate [m^3 s^{-1}]	Mean Liquid Residence Time [s]	Global Gas Holdup [-]	Separation Efficiency [-]
1	5.81×10^{-3}	43.8	0.33	1.00
1	7.75×10^{-3}	35.8	0.27	1.00
1	1.16×10^{-2}	25.5	0.22	1.00
1	1.36×10^{-2}	22.4	0.2	1.00
0.8	5.81×10^{-3}	30.5	0.53	1.00
0.8	7.75×10^{-3}	29.4	0.40	1.00
0.8	1.36×10^{-2}	19.3	0.31	1.00

Figure 3.6 shows the global gas holdup profile and liquid streamlines for a bubble diameter of 0.8 mm and an inlet liquid volumetric flow rate of 5.81×10^{-3} m^3 s^{-1}. Despite the high global gas holdup there are 3 distinct regions in its profile, additionally the induced swirl is visible in the liquid streamlines. As previously discussed, these characteristics are indicative of a separating system. These findings indicate that effective gas-liquid separation is possible at high gas holdups so long as the liquid volumetric flow rate is small enough to allow for sufficiently large mean liquid residence time.

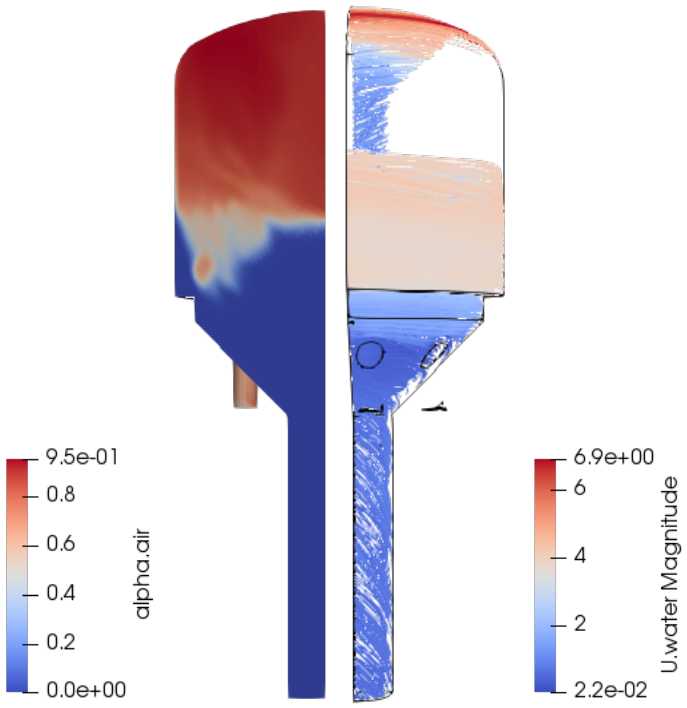

Figure 3.6: Gas Phase Holdup and Liquid Streamlines for a Liquid Volumetric Flow Rate of $5.81 \times 10^{-3} m^3 s^{-1}$. All Other Parameters Under Base Case Conditions as per Table 2.5.

3.2.5 Liquid Recycle Ratio

The impact of liquid recycle ratio is summarized in Table 3.3. As the liquid recycle ratio increases it is expected to reduce the liquid residence and restrict gas-liquid separation. As the recycle ratio increases more liquid is drawn into the recycle line, increasing the net downward velocity of the liquid. As the downward velocity of the liquid is increased the bubbles need a larger relative velocity to disengage and rise.

Table 3.3: Impact of Liquid Recycle Ratio on Flow Field and Separation Efficiency All Other Parameters Under Base Case Conditions as per Table 2.5.

Liquid Recycle Ratio	Mean Liquid Residence Time [s]	Global Gas Holdup [-]	Separation Efficiency [-]
0.50	30.1	0.27	1.00
0.60	29.1	0.30	1.00
0.70	28.0	0.33	1.00
0.80	24.0	0.42	1.00
0.90	13.0	0.70	0.00

The impact of liquid recycle ratio can also be visualized based on the spatial evolution of the global gas holdup shown in Figure 3.7. The gas-rich region grows as the liquid recycle ratio increases. When phase separation readily occurs, the gas holdup in the gas-rich region is around 90–95%, exhibiting small axial gradients as the region grows while the liquid-rich region similarly has liquid holdups near 100%. The region that exhibits the largest differences for separating systems is the conical section where liquid holdup varies between 0.6 and 1. The shape of this conical region is largely controlled by operating conditions, which impact the size of the gas-rich region but originates from the swirl induced by the flow entering via the offset elbow pipes. If operating conditions facilitate gas-liquid separation, such as Figure 3.7a, with a liquid recycle ratio of 0.5, the gas-rich region is relatively small allowing for a larger conical section to develop. Conversely, if the operating conditions are less favorable to bubble disengagement, the gas-rich region increases in size, and the height of the conical region decreases until non-existent. This phenomenon leads to an upset within the system where the separation efficiency then trends towards 0. The gas-to-liquid phase fraction at the pipe inlet is 1:1. As the separation efficiency trends toward 0, a similar phase fraction can be seen in the recycle line where there is gas rich core and a liquid rich region around the walls of the recycle line, see Figure 3.7e. Separating systems such as those pictured in Figure 3.7a-d have 3 distinct regions in the global gas holdup profile. Conversely, non-separating systems have a more uniform global gas holdup, see Figure 3.7e, where the feed composition is like that exiting through both outlets. Similar distinctions can be made for separating and non-separating systems with regards to the liquid streamlines. When the

system has a high separation efficiency the liquid streamlines have a clear swirling effect, which increasing the mean liquid residence time. However non-separating system exhibit strong axial recirculation zones.

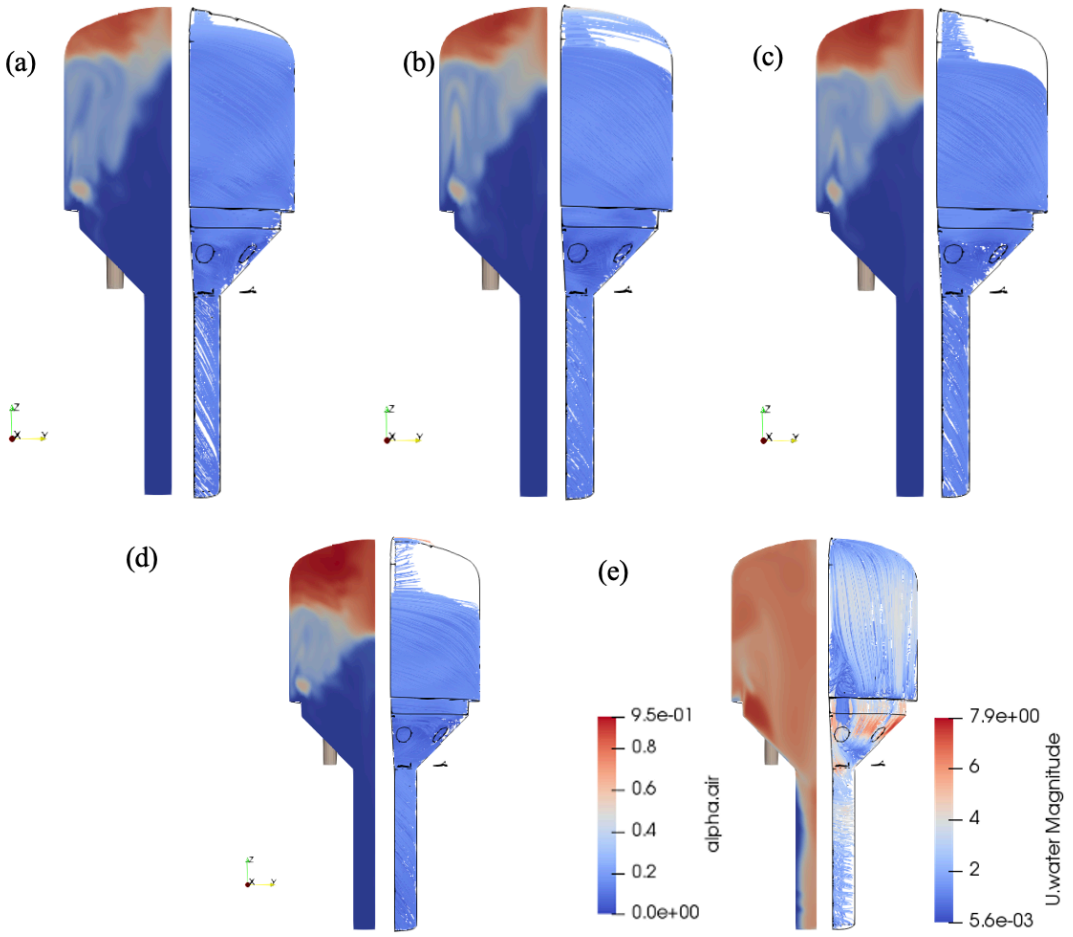

Figure 3.7: Gas Phase Holdup and Liquid Streamlines for Liquid Recycle Ratio of (a) 0.5 (b) 0.6 (c) 0.7 (d) 0.8 (e) 0.9. All Other Parameters Under Base Case Conditions as per Table 2.5.

The slip velocity in the recycle line, necessary for bubble escape at various liquid recycle ratios and velocities, was calculated to assess separation efficiency based on liquid velocity. The calculations consistently overpredicted the required bubble diameter for a high separation efficiency compared to CFD results. This indicates that the induced swirl in the active separation

zone significantly impacts separation efficiency, implying that it cannot be predicted solely by liquid velocity in the recycle line.

3.2.6 Viscosity

Increasing the viscosity is expected to increase the drag force on the bubble, which will reduce the relative velocity between the phases, hinder bubble disengagement from liquid streamlines, cause the bubbles to recirculate within the vessel, reduce the mean liquid residence time and ultimately hinder separation efficiency. This is under the assumption of a non-coalescing system where the bubble maintains a constant diameter. The impact of viscosity on mean liquid residence time is illustrated in Figure 3.8.

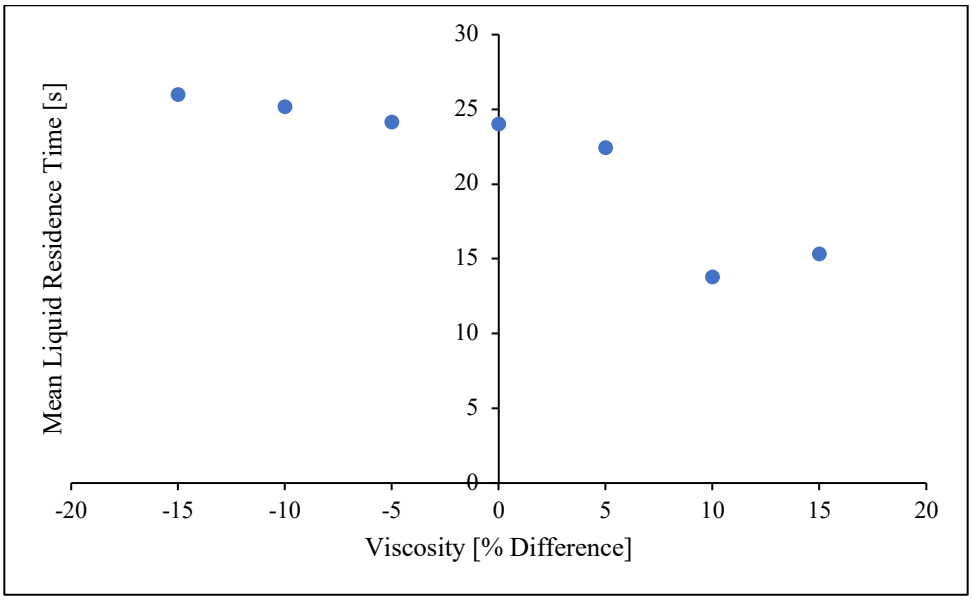

Figure 3.8: Impacts of Viscosity on Mean Liquid Residence Time

These results can also be interpreted visually, where both extreme liquid viscosity cases are shown in Figure 3.9. When the viscosity is decreased by 15%, the system has a high separation efficiency, indicated by the 3 distinct regions in the global has holdup profiles and swirl present in the liquid streamlines. However, when the liquid viscosity is increased by 15%, the system has a low separation efficiency, indicated by a relatively uniform global gas holdup profile and axial recirculation zones in the liquid streamlines.

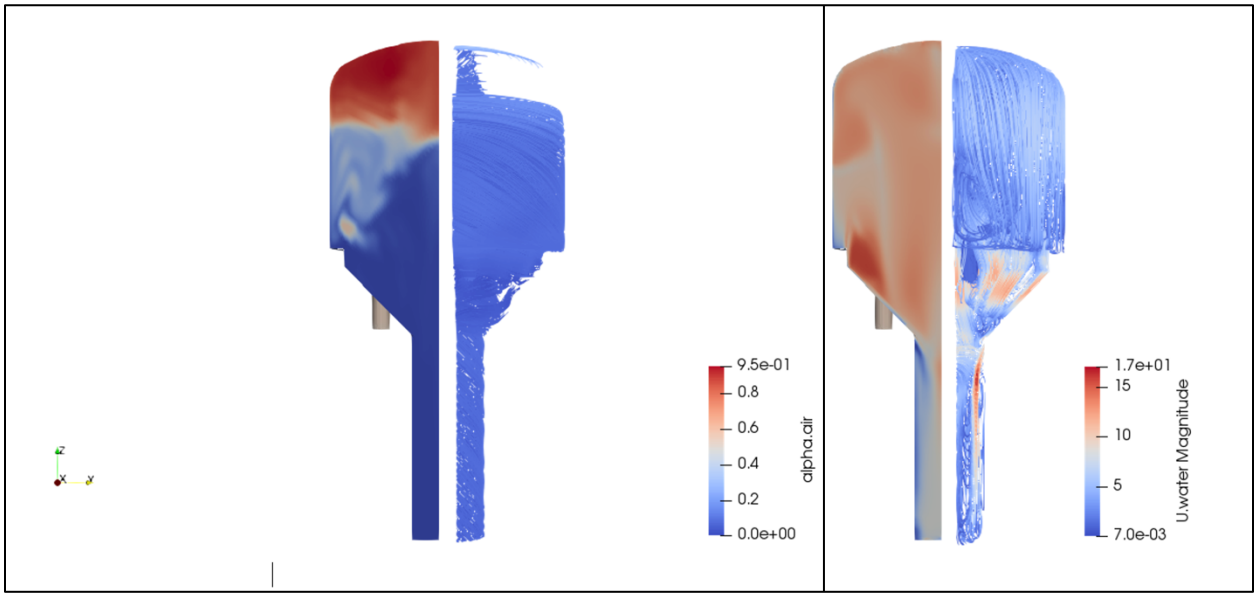

Figure 3.9: Global Gas Holdup and Liquid Streamlines for (a) Viscosity -15% and (b) Viscosity +15%. All Other Parameters Under Base Case Conditions as per Table 2.5.

3.2.7 Mean Liquid Residence Time

Figure 3.10, compares the mean liquid residence to the separation efficiency for all case studies presented. The figure shows a threshold developing ~ 18s, where simulations with a mean liquid residence time below 18s have a separation efficiency approaching 0 and simulations with a mean liquid residence time above 18s have a separation efficiency approaching 1. Notably, in the present investigation, separation efficiency manifests as a binary outcome: simulations when run to pseudo-steady state achieve a separation efficiency of approximately 1 or 0. This trend is supported through the analysis of the global gas holdup profiles and liquid streamlines. When the global gas holdup has 3 distinct regions, and the liquid streamlines exhibit the induced swirl introduced by the offset inlet pipes the separation efficiency approaches 1. As the gas-rich regions continues to grow, eventually it becomes level with pipe inlets and causing an upset, marked by the transformation of the global gas holdup to become more uniform throughout the vessel and the liquid streamlines to exhibit strong axial recirculation zones.

This binary nature of the separation efficiency is specific to our research framework with single bubble size simulations. If a bubble size distribution were introduced the separation efficiency is not expected to be binary. Unlike the discrete nature of separation efficiency, mean liquid residence time presents a continuous spectrum, offering a more nuanced understanding of trends as it nears different thresholds. Thus, employing mean liquid residence time as a metric allows for a comprehensive exploration of various parameter impacts on separation efficiency, fostering discussions centered on trends rather than solely binary outcomes.

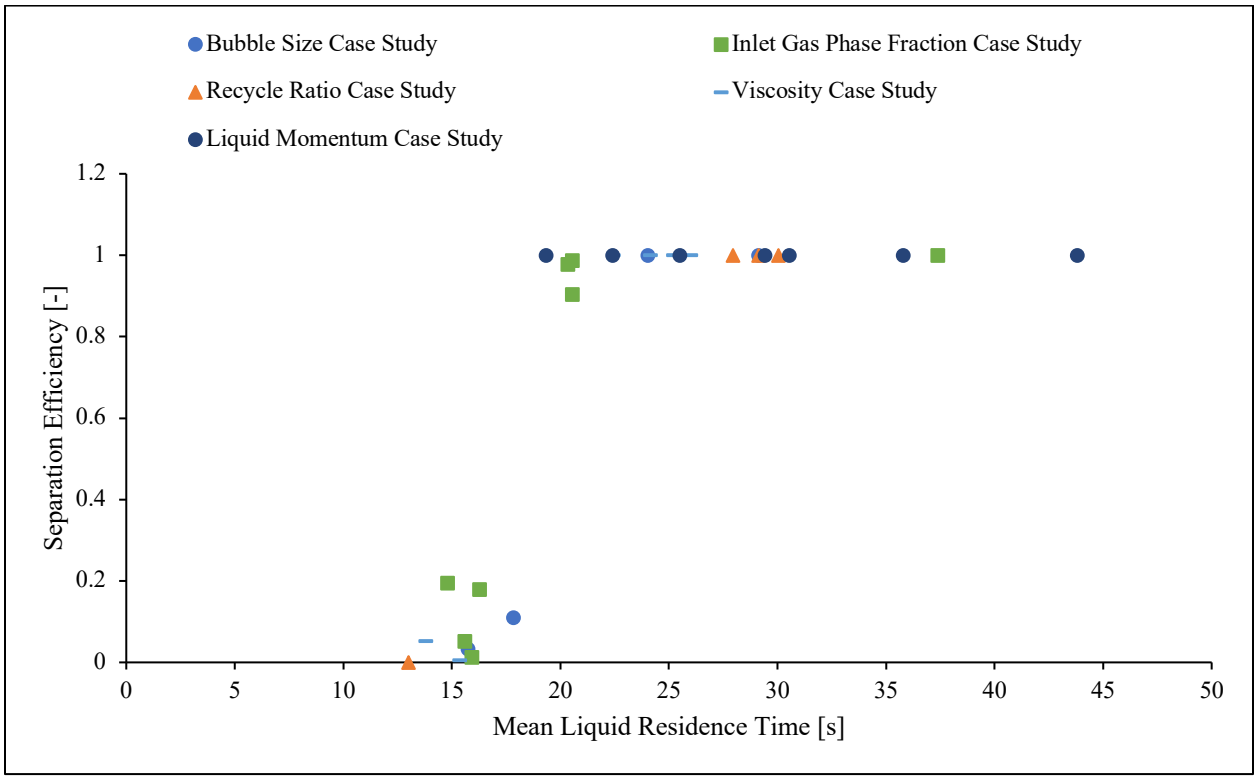

Figure 3.10: Separation Efficiency as Function of Mean Liquid Residence. All Simulated Cases.

Chapter 4

Conclusions

Through comprehensive studies employing the k-ω SST turbulence model in conjunction with the Tomiyama slightly contaminated drag model, this research has yielded insights into gas-liquid separation efficiency. The strategic selection of these models has ensured the stability and accuracy of our results, laying a solid foundation for future model comparisons incorporating inhomogeneous multiple size group population balance models.

Our investigations involved various case studies aimed at discerning the impacts of independent variables on gas-liquid separation efficiency. Notably, we observed that increasing bubble size led to enhanced separation efficiency, attributed to the larger buoyant force relative to drag. This facilitated the disengagement of larger bubbles from liquid streamlines, thereby improving separation. Furthermore, augmenting the inlet gas flow rate resulted in increased overall gas holdup, consequently reducing mean liquid residence time and, subsequently, gas-liquid separation efficiency. Although the influence of liquid momentum was less pronounced, its increase led to decreased mean liquid residence time, thereby impeding separation. Viscosity affects separation efficiency due to changes in drag exerted on bubbles and relative fluids velocities. Additionally, an increase in the liquid recycle ratio corresponded to decreased separation efficiency, likely due to reduced mean liquid residence time.

From above, the mean liquid residence time proved to be a consistent predictor of gas-liquid separation efficiency. In our diverse case studies encompassing variations in viscosity, bubble sizes, and recycle ratio, a mean liquid residence time exceeding 18 seconds consistently resulted in successful separation, whereas times below 18 seconds led to unsuccessful separation. This work contributes to the understanding of gas-liquid separation processes. By elucidating the intricate interplay of various parameters, our findings provide insights for optimizing separation efficiency in industrial applications. Moreover, the establishment of mean liquid residence time as a reliable predictor underscores its significance in process design and optimization endeavors.

References

Behzadi, A., Issa, R.I., Rusche, H., 2004. Modelling of dispersed bubble and droplet flow at high phase fractions. Chem. Eng. Sci. 59, 759–770. https://doi.org/10.1016/j.ces.2003.11.018

Boussinesq, J., 1877. Essai sur la théorie des eaux courantes.

Buffo, A., Vanni, M., Renze, P., Marchisio, D.L., 2016. Empirical drag closure for polydisperse gas–liquid systems in bubbly flow regime: Bubble swarm and micro-scale turbulence. Chem. Eng. Res. Des. 113, 284–303. https://doi.org/10.1016/j.cherd.2016.08.004

Burns, A.D., Frank, T., Hamill, I., Shi, J.-M., 2004. The Favre Averaged Drag Model for Turbulent Dispersion in Eulerian Multi-Phase Flows.

Drew, D.A., Passman, S.L., 1998. Theory of Multicomponent Fluids.

Eccles, R.M., 1993. Residue hydroprocessing using ebullated-bed reactors. Fuel Process. Technol. 35, 21–38. https://doi.org/10.1016/0378-3820(93)90083-G

Ishii, M., Zuber, N., 1979. Drag coefficient and relative velocity in bubbly, droplet or particulate flows. AIChE J. 25, 843–855. https://doi.org/10.1002/aic.690250513

Jones, W.P., Launder, B.E., 1972. The prediction of laminarization with a two-equation model of turbulence. Int. J. Heat Mass Transf. 15, 301–314. https://doi.org/10.1016/0017-9310(72)90076-2

Lahey, R.T., 2005. The simulation of multidimensional multiphase flows. Nucl. Eng. Des. 235, 1043–1060. https://doi.org/10.1016/j.nucengdes.2005.02.020

Lane, C.D., Macchi, A., McKnight, C.A., Wiens, J., Donaldson, A.A., 2019a. Internal Gas–Liquid Separation in Industrial Ebullated Bed Hydroprocessors. Ind. Eng. Chem. Res. 58, 18675–18683. https://doi.org/10.1021/acs.iecr.9b02201

Lane, C.D., Macchi, A., Pjontek, D., McKnight, C.A., Wiens, J., Donaldson, A.A., 2019b. Modeling the Fluid Dynamics of a Commercial Ebullated Bed Hydroprocessor. Ind. Eng. Chem. Res. 58, 18387–18396. https://doi.org/10.1021/acs.iecr.9b02779

Lane, C.D., McKnight, C.A., Wiens, J., Reid, K., Donaldson, A.A., 2016a. Parametric analysis of internal gas separation within an ebullated bed reactor. Chem. Eng. Res. Des. 105, 44–54. https://doi.org/10.1016/j.cherd.2015.10.043

Lane, C.D., Parisien, V., Macchi, A., Donaldson, A.A., 2016b. Investigation of bubble swarm drag at elevated pressure in a contaminated system. Chem. Eng. Sci. 152, 381–391. https://doi.org/10.1016/j.ces.2016.06.017

Launder, B.E., 1995. Turbulence Modelling for CFD. By D. C. WILCOX. DCW Industries Inc., 1993. 460pp. $75. J. Fluid Mech. 289, 406–407. https://doi.org/10.1017/S0022112095211388

Lehnigk, R., Bainbridge, W., Liao, Y., Lucas, D., Niemi, T., Peltola, J., Schlegel, F., 2022. An open-source population balance modeling framework for the simulation of polydisperse multiphase flows. AIChE J. 68, e17539. https://doi.org/10.1002/aic.17539

Liao, Y., Ma, T., Krepper, E., Lucas, D., Fröhlich, J., 2019. Application of a novel model for bubble-induced turbulence to bubbly flows in containers and vertical pipes. Chem. Eng. Sci. 202, 55–69. https://doi.org/10.1016/j.ces.2019.03.007

Liao, Y., Ma, T., Liu, L., Ziegenhein, T., Krepper, E., Lucas, D., 2018. Eulerian modelling of turbulent bubbly flow based on a baseline closure concept. Nucl. Eng. Des. 337, 450–459. https://doi.org/10.1016/j.nucengdes.2018.07.021

Liao, Y., Rzehak, R., Lucas, D., Krepper, E., 2015. Baseline closure model for dispersed bubbly flow: Bubble coalescence and breakup. Chem. Eng. Sci. 122, 336–349. https://doi.org/10.1016/j.ces.2014.09.042

Lopez de Bertodano, M., Lahey, R., JONES, O., 1994. DEVELOPMENT OF A K-EPSILON MODEL FOR BUBBLY 2-PHASE FLOW. J. Fluids Eng. 116, 128–134.

Ma, T., Santarelli, C., Ziegenhein, T., Lucas, D., Fröhlich, J., 2017. Direct numerical simulation–based Reynolds-averaged closure for bubble-induced turbulence. Phys. Rev. Fluids 2. https://doi.org/10.1103/PhysRevFluids.2.034301

Mach, J., Parisien, V., Wiens, J., McKnight, C., Macchi, A., 2020a. Impact of plenum conditions and gas-liquid distributor on bubble column hydrodynamics 211. https://doi.org/10.1016/j.ces.2019.115296

Mach, J., Parisien, V., Wiens, J., McKnight, C.A., Macchi, A., 2020b. Impact of plenum conditions and gas-liquid distributor on bubble column hydrodynamics. Chem. Eng. Sci. 211, 115296. https://doi.org/10.1016/j.ces.2019.115296

Magolan, B., Lubchenko, N., Baglietto, E., 2019. A quantitative and generalized assessment of bubble-induced turbulence models for gas-liquid systems. Chem. Eng. Sci. X 2, 100009. https://doi.org/10.1016/j.cesx.2019.100009

McKnight, C.A., Hackman, L.P., Grace, J.R., Macchi, A., Kiel, D., Tyler, J., 2003. Fluid Dynamic Studies in Support of an Industrial Three-Phase Fluidized Bed Hydroprocessor. Can. J. Chem. Eng. 81, 338–350. https://doi.org/10.1002/cjce.5450810302

Menter, F., Kuntz, M., Langtry, R., 2003. Ten years of industrial experience with the SST turbulence model. Heat Mass Transf. 4.

Menter, F.R., 2009. Review of the shear-stress transport turbulence model experience from an industrial perspective. Int. J. Comput. Fluid Dyn. 23, 305–316. https://doi.org/10.1080/10618560902773387

Menter, F.R., 1994. Two-equation eddy-viscosity turbulence models for engineering applications. AIAA J. 32, 1598–1605. https://doi.org/10.2514/3.12149

Moukalled, F., Mangani, L., Darwish, M., 2016. The Finite Volume Method in Computational Fluid Dynamics. Springer, New York. https://doi.org/10.1007/978-3-319-16874-6

Mowla, A., Agnaou, M., Treeratanaphitak, T., Budman, H.M., Abukhdeir, N.M., Ioannidis, M.A., 2023. Gas segregation in a pilot-scale ebullated bed system: Experimental investigation and model validation. Chem. Eng. Res. Des. 194, 742–755. https://doi.org/10.1016/j.cherd.2023.05.024

Pjontek, D., 2014. Fluid Dynamic Studies in Support of an Industrial Ebullated Bed Hydroprocessor.

Pjontek, D., Donaldson, A., Macchi, A., 2020. Three-Phase (Gas–Liquid–Solid) Fluidization, in: Essentials of Fluidization Technology. John Wiley & Sons, Ltd, pp. 553–589. https://doi.org/10.1002/9783527699483.ch22

Politano, M.S., Carrica, P.M., Converti, J., 2003. A model for turbulent polydisperse two-phase flow in vertical channels. Int. J. Multiph. Flow 29, 1153–1182. https://doi.org/10.1016/S0301-9322(03)00065-X

Pope, S., 2020. Turbulent Flows. Cambridge University Press, Cambridge, UK.

Rzehak, R., Krepper, E., 2013. Bubble-induced turbulence: Comparison of CFD models. Nucl. Eng. Des. 258, 57–65. https://doi.org/10.1016/j.nucengdes.2013.02.008

Schiller, Naumann, 1934. A drag coefficient correlation 77, 318.

Schlegel, F., Bilde, K.G., Draw, M., Evdokimov, I., Hänsch, S., Kamble, V.V., Khan, H., Krull, B., Lehnigk, R., Li, J., Lyu, H., Meller, R., Petelin, G., Tekavčič, M., 2022. HZDR Multiphase Addon for OpenFOAM. https://doi.org/10.14278/rodare.1742

Song, S.X., Kuehne, D.L., Kemoun, A., Reynolds, B., 2014. Apparatus and Method for Hydroconversion. EP2718406A2.

Tas-Koehler, S., Liao, Y., Hampel, U., 2021. A critical analysis of drag force modelling for disperse gas-liquid flow in a pipe with an obstacle. Chem. Eng. Sci. 246, 117007. https://doi.org/10.1016/j.ces.2021.117007

Tomiyama, A., Kataoka, I., Zun, I., Sakaguchi, T., 1998. Drag Coefficients of Single Bubbles under Normal and Micro Gravity Conditions. JSME Int. J. Ser. B 41, 472–479. https://doi.org/10.1299/jsmeb.41.472

Totten, J., 2019. Modeling of plenumn chamber and grid hydrodynamics in a commercial ebullated bed hydroprocessor.

Troshko, A.A., Hassan, Y.A., 2001. A two-equation turbulence model of turbulent bubbly flows. Int. J. Multiph. Flow 27, 1965–2000. https://doi.org/10.1016/S0301-9322(01)00043-X

Versteeg, H.K., Malalasekera, W., 2007. An introduction to computational fluid dynamics: the finite volume method, 2nd ed. ed. Pearson Education Ltd, Harlow, England ; New York.

Wellek, R.M., Agrawal, A.K., Skelland, A.H.P., 1966. Shape of liquid drops moving in liquid media. AIChE J. 12, 854–862. https://doi.org/10.1002/aic.690120506

Yeoh, G.H., Tu, J. (Eds.), 2010. , in: Computational Techniques for Multiphase Flows. Butterworth-Heinemann, Oxford, pp. 627–643. https://doi.org/10.1016/B978-0-08-046733-7.00015-1